



aerosol brought up to cloud base (Seinfeld et al., 2016) and is the main determinant of supersaturation (Sullivan et al., 2016), which controls aerosol activation, thus, defining CCN spectra and cloud droplet number at cloud base (Calmer et al., 2018; Conant et al., 2004). Updrafts tend to narrow cloud droplet concentration spectra (Sardina et al., 2018). Humidity fluctuations can also influence the amount of aerosol activation under certain circumstances (Prabakharan et al., 2020).

Aerosols in marine boundary layers can be sourced locally (e.g., sea salt) or, if near shore, from continental pollution advected in either the boundary layer or in the free troposphere and entrained into the boundary layer. This was a focus of the second Aerosol Characterization Experiment undertaken in 1997 over the subtropical North-eastern Atlantic Ocean. Raes et al. (1997) and Van Dingenen et al. (2000) found that such transport of pollution is important in defining the size distribution of boundary layer aerosols. If a cloud is present, Jia et al. (2019) found from Variability of the American Monsoon Ocean-Cloud-Atmosphere Land Study Regional Experiment data that aerosol entrained into the boundary layer from the free troposphere has little effect on the cloud. Rather, it is the entrainment of warm, dry air from above that really impacts the cloud. During cold air outbreaks (CAOs) over the WNAO, the entrainment of free tropospheric air results in a reduction of CCN concentration that leads to the transition from closed to open cellular convection (Tornow et al., 2022).

Turbulence, aerosols, and cloud microphysics need to be parameterized in ESMs like the Community Earth System Model version 2 (CESM2), because these processes occur at scales smaller than the model grid cell, typically at a resolution of  $\sim 1 \times 1$ . The simulated uncertainty in clouds and aerosols comes about because of the differences in these parameterizations between ESMs.

A common way to represent boundary layer turbulence in ESMs is the eddy-diffusivity (ED) approach. In such a scheme, turbulent mixing is represented as a diffusive process in which turbulent fluxes are proportional to the vertical gradients of mean quantities, but a countergradient term is added to account for the transport due to dry convection (e.g., Holtslag & Boville, 1993). The ED approach is problematic in the presence of moist convection (e.g., shallow cumulus) (Teixeira et al., 2020). Bretherton and Park (2009) attempted to deal with this by adapting the classical ED parameterization to operate on cloud conserved quantities, that is, the liquid-ice static energy and total specific humidity. Another recent approach to dealing with moist convection is eddy diffusivity mass flux (EDMF) in which boundary layer turbulence is decomposed into that due to organized convective updrafts represented by mass fluxes and background turbulence represented by eddy diffusivity (Siebesma et al., 2007). The mass flux representation for convective updrafts is similar to the parameterizations used to represent shallow and deep convection (e.g., Arakawa & Schubert, 1974; Zhang & McFarlane, 1995).

The development of EDMF is part of a movement toward unifying the representation of convection and boundary layer turbulence in model parameterizations. This is the basis for the development of higher-order schemes like the Cloud Layers Unified by Binormals (CLUBB; Golaz et al., 2002) or the Simplified Higher Order Closure (Bogenschutz & Krueger, 2012). Such higher-order schemes need to assume bivariate probability distribution functions (PDFs) to close some turbulent quantities like the covariances between vertical velocity and conservative quantities, like liquid potential temperature and total water content. CLUBB has been implemented into CESM2 and the Energy Exascale Earth System Model (E3SM), unifying boundary layer turbulence, shallow convection, and cloud macrophysics in those ESMs. As the name suggests, CLUBB PDFs are assumed to be binormal, which was confirmed in the parameterization's development by aircraft observations (Larson et al., 2002) and large eddy simulation (LES) results (Larson & Golaz, 2005) for mostly subtropical stratocumulus and trade wind cumulus. Larson and Golaz (2005) also confirm the binormal PDF for a clear boundary layer using LES. While such tests suggest a universality of the binormal assumption, this has yet to be independently verified using observations over other regions.

Here, we use the aircraft measurements made during the first year of flights from the Aerosol Cloud Meteorology Interactions over the Western Atlantic Experiment (ACTIVATE; Sorooshian et al., 2019) during February and March and August and September 2020. While the focus of ACTIVATE is to study ACI, the low-flying Falcon aircraft had a high-temporal resolution (20 Hz) meteorological instrument on board, which we use to characterize the cloud-topped boundary layer (CTBL) and boundary layers devoid of clouds. We want to leverage the full set of level leg data rather than just a few ideal cases. Such characterizations can be used to evaluate the turbulence simulated by model parameterizations like CLUBB. We also include LES here to act as a bridge between the surface measurements and the global ESM simulations; the LES is initiated and forced by observed conditions,

unlike the global simulations presented here. LES has been used to evaluate global ESMs (e.g., Atlas et al., 2020) and was used in the development of CLUBB (Larson & Golaz, 2005).

The region of interest for ACTIVATE is the western North Atlantic Ocean (WNAO) off the East Coast of the United States (U.S.). Corral et al. (2021) provide an overview of the atmospheric chemistry that impacts the region and the coast. Painemal et al. (2021) described the climatology of atmospheric circulation, boundary layer and cloud structure, and precipitation in the region. Reanalyses have too wide of a Gulf Stream along with some other small biases in the region (Seethala et al., 2021). This region is particularly prone to CAOs, events of cold air moving across the warm waters of the WNAO behind synoptic cyclones when westerlies are enhanced. These can occur from September to May but occur 5–7 days per month from November to March, with a peak in January and February. The core of these events occurs over the Gulf Stream (Painemal et al., 2021). CAOs can be identified on satellite imagery by streets of clouds along the direction of the wind (Atlas et al., 1983). Furthermore, clouds over the WNAO are characterized by higher cloud droplet concentrations during strong CAOs (Dadashazar et al., 2021). Shallow cumulus is the dominant weather regime over the WNAO throughout the year, especially over the Gulf Stream (Painemal et al., 2021), as defined by cloud structure and atmospheric conditions (Tselioudis et al., 2013). Wintertime clouds in this region can contain ice, which can accelerate cloud breakup (Tornow et al., 2021).

Since CAOs are particularly prevalent in winter (Painemal et al., 2021), such events are a particular focus of ACTIVATE's winter deployments. An early field study of CAOs was undertaken over the western North Pacific Ocean centered over Okinawa, Japan during the Air Mass Transformation Experiment (AMTEX) in 1974 and 1975 (Lenschow & Agee, 1976). CAOs have also been investigated previously over the western North Atlantic. The Mesoscale Air-Sea Exchange Experiment occurred in January 1983 (Boers & Melfi, 1987), relying heavily on lidar measurements (Melfi et al., 1985), and several flights of the Genesis of Atlantic Lows Experiment conducted in February 1986 focused on understanding CAO processes (Dirks et al., 1988). In particular, the air-sea interaction during CAOs observed during GALE was the focus in Bane and Osgood (1989), Vukovich et al. (1991), and Grossman and Betts (1990). More recently, CAOs were investigated in the second special observation period of the hydrological cycle in the Mediterranean Experiment over the Mediterranean Sea (Brilouet et al., 2020), over the North Sea in Abel et al. (2017), and during the Southern Ocean Clouds, Radiation, and Aerosol Transport Experimental Study (Atlas et al., 2020).

The focus of many of these studies is on understanding the apparent stratocumulus-to-cumulus transition that CAO-induced clouds undergo as the air moves further offshore. These include observational and modeling (LES and single column model (SCM)) studies. Abel et al. (2017) was a recent observational study that found that precipitation was fundamental to this transition in a North Sea CAO. Tornow et al. (2021) found this as well in the LES of a WNAO CAO, adding that ice was instrumental in initiating the precipitation.

The analogy is often made between the transition in CAO-induced clouds and the well-studied subtropical stratocumulus-to-trade wind cumulus. This was the focus of the LES and SCM intercomparisons undertaken for the Global Energy and Water Cycle Exchanges Project, Global Atmospheric System Studies, and European Union Cloud Intercomparison, Process Study and Evaluation Project (de Roode et al., 2016; Neggers et al., 2017; van der Dussen et al., 2013). However, the dominant weather regime over the WNAO is that of cumulus (Painemal et al., 2021). Thus, it may be more appropriate to call this transition of WNAO clouds from overcast to broken clouds, as described by Tornow et al. (2021), or from rolls to open and closed cells (Atkinson & Zhang, 1996). Indeed, daily mean clouds and the Earth's Radiant Energy System satellite-derived low cloud fraction are generally maximum just offshore for the flight days in the first deployment of ACTIVATE in February and March 2020. For the days of the second deployment in August and September, the low cloud fraction is low, consistent with the trade wind cumulus regime.

We briefly describe ACTIVATE and the meteorological instrumentation used on the Falcon in the next section. Section 3 describes the methodology to derive turbulent quantities. The results from the turbulence characterization are elaborated in Section 4. Further discussion of the results and conclusions are given in Section 5.

## 2. ACTIVATE

ACTIVATE is obtaining detailed, simultaneous, and systematic measurements of aerosol particles and clouds from in situ and remote sensing instruments deployed on two coordinated aircraft over six deployments between

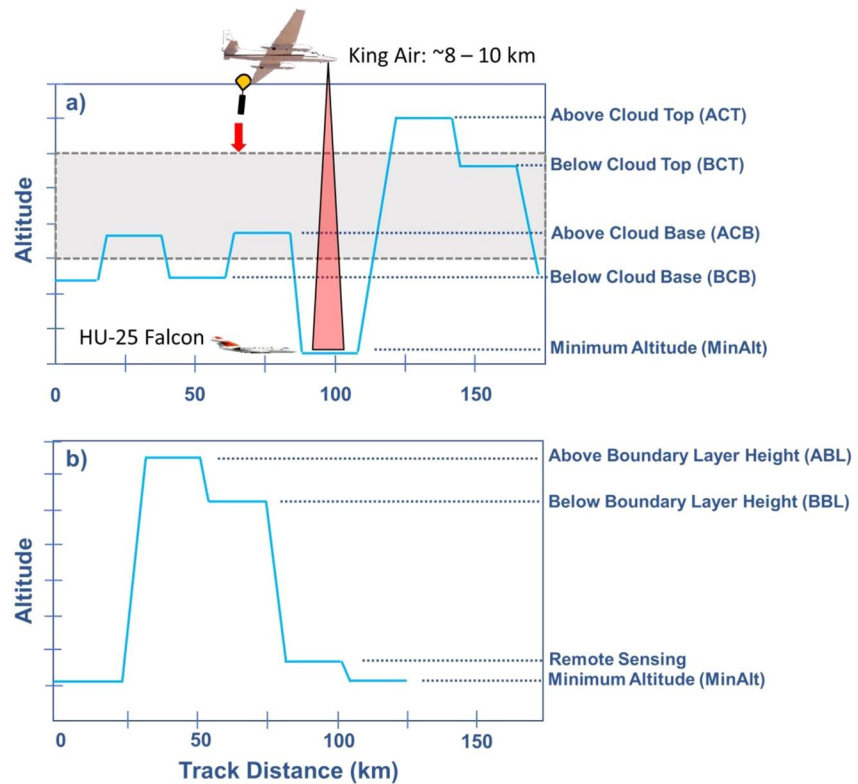


**Figure 1.** The level legs performed in the cloudy (a) and clear (b) ensembles during aerosol cloud meteorology interactions over the western Atlantic experiment. The blue line represents an example track of the HU-25, and the cloud layer is represented by the gray.

2020 and 2022 (Sorooshian et al., 2019). The sampling strategy is built around developing a large volume of data to enhance statistical analysis of aerosol-cloud-meteorology interactions. Flights are conducted over the WNAO to capitalize on the wide spectrum of aerosol and meteorological conditions in different seasons conducive to wide dynamic ranges in parameters relevant to ACI (Corral et al., 2021; Painemal et al., 2021; Sorooshian et al., 2020). The focus of this work is on data collected in the first two deployments in 2020 (14 February–12 March and 13 August–30 September). An HU-25 Falcon flies underneath a King Air to conduct in situ sampling of boundary layer clouds with a payload of instruments characterizing aerosol particles, gases, clouds, and meteorological parameters including winds. The King Air flies at  $\sim 8\text{--}10$  km with a payload comprised of a Research Scanning Polarimeter (RSP) and the High Spectral Resolution Lidar (HSRL-2) to characterize aerosol and cloud properties from above. Dropsondes are also deployed from the King Air to measure profiles of atmospheric state parameters.

The majority of flights ( $\sim 90\%$ ) are referred to as “statistical surveys” that involve out-and-back flights from the base of operations at NASA Langley Research Center. During these flights, the Falcon repeatedly conducts the same series of legs, the collection of which is referred to as an ensemble, to obtain vertically resolved data below, in, and above clouds (Figure 1a). Each cloud ensemble is comprised of the following level legs: above cloud top (ACT), below cloud top (BCT), above cloud base (ACB), below cloud base (BCB), and the minimum altitude (MinAlt) that the Falcon can fly at ( $\sim 150$  m). Ensembles are also made in cloud-free conditions that include the above boundary layer top (ABL), below boundary layer top (BBL), and a remote sensing leg (RS) to facilitate intercomparisons with King Air instruments at  $\sim 240$  m and MinAlt ( $\sim 150$  m) (Figure 1b). Here, we focus on the ABL, BBL, and MinAlt legs for the clear ensembles. Typical flight durations are  $\sim 200$  min, with either one or two flights per flight day. Level legs are typically  $\sim 4$  min in duration or  $\sim 25$  km in length.

The winds on the HU-25 are measured by the NASA Langley Turbulent Air Motion Measurement System (TAMMS). The primary components include fast-response flow-angle and temperature sensors to determine the wind with respect to the aircraft along with an Applanix 650 inertial navigation system (Applanix Inc.) to

provide the aircraft's position, speed, and attitude. The aircraft platform velocity components are computed internally by the Applanix by combining the GPS and inertial data via a Kalman filtering technique. The horizontal components ( $u$  and  $v$ ) are truly zonal and meridional; vertical wind speeds ( $w$ ) are positive upwards. The data are recorded at 200 Hz on a UEIPAC-300 real time controller (United Electronics Industries) and then averaged down to 20 Hz for processing, analysis, and data archiving. The flow-angle system includes five, flush-mounted pressure ports installed in a cruciform pattern in the aircraft radome to provide angle of attack (vertically aligned ports) and sideslip (horizontally aligned ports) measurements. Corresponding fast-response, high-precision pressure transducers are placed as close as possible to the pressure ports in order to minimize delays and errors. Pitch and yaw maneuvers, speed variations, and reverse headings are performed periodically during deployments to verify system operation and calibration and validate derived mean horizontal-wind vectors. Three-dimensional winds are computed from the full air motion equations (Lenschow, 1986). Ambient air temperature measurements needed to determine true air speed are made with a Rosemount Model 102 nondeiced total air temperature sensor with a fast-response platinum sensing element (E102E4AL). The total, static, and dynamic (impact) pressures are measured off of the co-pilot's pressure port with the use of a Rosemount pressure transducer and a Rosemount Micro Air Data Transducer (MADT model 2014MA1A). Dew point temperature is measured by an EdgeTech model 137 Chilled Mirror Hygrometer. This setup has been used extensively for other campaigns on the NASA P-3 aircraft. Additional details on the instrumentation, calibration, and intercomparison results of the TAMMS when used on the NASA P-3 can be found at Thornhill et al. (2003).

Since this is the initial implementation of TAMMS on the NASA HU-25, and while the same calibration coefficients cannot be ported from one aircraft to another, the calibration maneuvers can be used independent of aircraft type. A series of calibration flights have been performed throughout the campaigns to determine the angle of attack slope and offset (speed variations), sideslip slope (tailwags/crabbing), and reverse headings to determine the heading offset (crosswind reverse heading) and the pressure defect (alongwind). They were done above the marine boundary layer, in clean, homogenous air masses at various altitudes up to 15 kft. Due to the removal of the Applanix post each campaign, the heading offset changed from year to year. The calibration results of the speed variations and sideslips for all three years of the ACTIVATE program are provided in Figures S1 and S2 in Supporting Information S1, respectively. They show that both the angles of attack and sideslip vary linearly with pitch and, yaw respectively, and that the results are repeatable from year to year and calibration to calibration, regardless of altitude. A Fourier power spectra for a three-minute segment in the marine boundary layer is shown in Figure S3 in Supporting Information S1. It shows that the derived vertical winds show the desired  $-5/3$  falloff all the way down to 10 Hz with no noticeable noise interference. When all calibrations are applied to the calculations of the horizontal winds, the wind speed and direction will be independent of the aircraft heading.

To investigate how turbulence impacts ACI, we also use data from the aerosol and cloud droplet probes on board the HU-25. These are provided by the Langley Aerosol Research Group (LARGE) instrument suite, which includes probes to measure ultrafine, total, and nonvolatile aerosol number densities and cloud condensation number (CCN) concentrations, cloud particle size, and to collect liquid water among others (<https://science-data.larc.nasa.gov/large/>). Cloud droplet number concentrations are also measured by the Fast Cloud Droplet Probe (FCDP) (Knop et al., 2021). Rain water content is derived from the two-dimensional stereo (2DS) instrument (SPEC Inc.) Total aerosol number concentrations are integrated for diameters  $>10$  nm.

We also use measurements from the HSRL-2 and RSP onboard the King Air. Mixed layer height (MLH) is estimated from HSRL-2 measurements during clear sky conditions (Scarino et al., 2014). Aerosol MLHs, which are a good proxy for boundary layer heights during the daytime, were derived by identifying sharp gradients in vertically resolved profile measurements of aerosol backscatter at 532 nm. Since 2006, HSRL-derived MLHs have been used to evaluate modeled boundary layer heights, as well as be used as a constraint for measured and modeled parameters.

Cloud fraction is derived from an RSP cloud test-passed product. This data containing five bits, each representing a different cloud type. We rely on bits 2 and 4 which refer to low-level clouds over water. Cloud fraction was found by dividing the number of times bits 2 and 4 found clouds by the total number of samples.

### 3. Methods

There is a several decade long history of obtaining turbulence measurements from aircraft. For instance, Lenschow et al. (1980) studied the turbulence measurements from AMTEX, investigating the applicability of known scaling

laws and budget analyses during CAOs. Such an analysis largely relies on vertical profiling legs (e.g., Jen-La Plante et al., 2016; Lenschow et al., 1988; Tjernström, 1993). Most recently, Dodson and Small Griswold (2021) and Nowak et al. (2021) investigated turbulence measured in both level legs and vertical profiles.

Since most of the sampling during ACTIVATE occurs during level legs during the vast majority of statistical surveys, we focus on analyzing the turbulence from the flights in each of the level legs for cloudy and clear ensembles except for takeoff, landing, and transit during the winter and summer deployment flights in 2020. The turbulent perturbations of the zonal and meridional ( $u'$  and  $v'$ , respectively) and vertical ( $w'$ ) wind speeds are calculated by subtracting the leg means from the 20-Hz TAMMS data. Wind variances are calculated as the leg means of the square of the turbulent perturbations of wind components ( $\langle u'^2 \rangle$ ,  $\langle v'^2 \rangle$ , and  $\langle w'^2 \rangle$  where  $\langle \rangle$  indicates an average over a certain period of time). Thus, TKE is calculated as:

$$\text{TKE} = \frac{1}{2} (\langle u'^2 \rangle + \langle v'^2 \rangle + \langle w'^2 \rangle) \quad (1)$$

The skewness of the vertical velocity is defined as:

$$Sk_w = \frac{\langle w'^3 \rangle}{(\langle w'^2 \rangle)^{3/2}} \quad (2)$$

where  $\langle w'^3 \rangle$  is the third moment. The skewness in scalars (i.e., total water content  $q_t$  and liquid potential temperature  $\theta_l$ ) is defined in respect to  $Sk_w$  (Larson, 2017; Larson & Golaz, 2005).

Despite our focus on the level legs, our goal here is to use the ACTIVATE observations to aid in the evaluation of ESM simulated turbulence. Because it is not really possible to define similar level legs in the coarse horizontal and vertical resolution of ESM grid boxes, we also use the vertical profiles from the nonlevel legs (i.e., ascents, descents, and spirals). Average profiles of meteorological quantities of wind speed, potential temperature, and specific humidity are derived from averaging the observational data across 30 m elevation bins. Similarly, vertical profiles of turbulent quantities are found by finding perturbations across the same 30 m elevation bins.

Similar to the wind perturbations, we also calculate perturbations in virtual potential temperature  $\theta_v$  and liquid potential temperature  $\theta_l$  along with those of specific humidity  $q$  and total water content  $q_t$  such that

$$\theta_v \approx \theta(1 + 0.61q) \quad (3)$$

$$\theta_l \approx \theta - \frac{\theta L_v q_l}{C_p T} \quad (4)$$

where  $C_p$  is the specific heat of air at constant pressure,  $q$  is found from the measured temperature and dew point, and

$$q_t = q + q_l \quad (5)$$

where  $q_l$  is the liquid water content, assuming that the cloud is completely liquid.

From these, the covariances between vertical velocity and virtual potential temperature ( $\langle w'\theta_v' \rangle$ ) and between vertical velocity, water vapor specific humidity ( $\langle w'q' \rangle$ ), and total water content ( $\langle w'q_t' \rangle$ ) are also determined. As in Dodson and Small Griswold (2021), these are converted to energy fluxes:

$$F_b = \bar{\rho} C_p \langle w'\theta_v' \rangle, \quad (6)$$

$$F_q = \bar{\rho} L_v \langle w'q' \rangle, \quad \text{and} \quad (7)$$

$$F_{q_t} = \bar{\rho} L_v \langle w'q_t' \rangle \quad (8)$$

where  $\bar{\rho}$  is the mean air density,  $C_p$  is the specific heat of air, and  $L_v$  is the latent heat of vapourization.

Frequency distributions of the above turbulent wind variances, TKE,  $Sk_w$ , and fluxes are found from the number of occurrences within bins of fixed width for each of the level legs for cloudy ensembles during the winter and summer flights and clear ensembles for the summer flights. As there were only four clear ensembles sampled during the winter deployment, cloud-free boundary layers are not investigated here. The various distributions are summarized by the medians, means, and interquartile ranges (IQRs) (i.e., the 25th to 75th percentiles).

We further determine if the observed frequency distributions have any relevance to model evaluation by comparing them to those found from simulations from the atmosphere models in CESM2 (Danabasoglu et al., 2020) and E3SMv2 (E3SM Project, DOE, 2021), that is, the Community Atmosphere Model version 6 (CAM6) and the E3SM Atmosphere Model version 2 (EAMv2), respectively. Both of these models use the higher-order scheme CLUBB that unifies boundary layer turbulence, shallow convection, and cloud macrophysics. The main difference in the CLUBB implementation between these two models is that EAMv2 recently underwent a retuning of the parameters used to define the width of the binormal PDFs as well as the effects of the turbulence skewness  $Sk_w$  in the determination of quantities (Ma et al., 2021). This retuning was undertaken to improve the simulation of the subtropical stratocumulus decks. These two ESMs also utilize the same algorithms for the representation of cloud microphysics (Gettelman & Morrison, 2015) and to calculate surface turbulent fluxes (Large & Pond, 1982) as well as the same four model aerosol (MAM-4).

The simulations presented here are active atmosphere-land simulations, in which sea surface temperature is prescribed from observations. Both models are spun up for three months from October 2002 by nudging the model vertical profiles toward those in the Modern-Era Retrospective Analysis for Research and Applications version 2 (Gelaro et al., 2017). From January 2003, the model has run normally without being nudged; this is the ongoing main simulation with the usual monthly mean output. This is not sufficient to diagnose problems in the model. Therefore, branch simulations are initialized at specific times from the ongoing main simulation to produce enhanced instantaneous output at the resolution of the 30-min time steps. These branches were run for 15 days from 19 February to 5 March and 22 August–5 September beginning in 2004 (after the main simulation is allowed to relax from the nudging for a whole year) until 2010. The frequency distributions are derived from all ocean grid cells between 32° and 40°N and 67°–77°W, which geographically encompass all of the ACTIVATE flight tracks from 2020 during day time steps between 0600 and 1800 local time.

Verification of the juxtaposition of observations with the ESM simulation results is also assisted via comparison to Weather Research and Forecasting model (Skamarock et al., 2019) run inLES mode (Wang & Feingold, 2009). Three simulations were performed for the process study days of 28 February, 1 March, and 2 June 2020. The domain for these simulations was 60 × 60 km with a horizontal resolution of 300 m. Model top was located at 7 km with 153 layers with a vertical resolution in the boundary layer of 33 m. Li et al. (2022) describe these LES runs in more detail.

## 4. Results

### 4.1. Meteorological Context

The flight tracks of the ACTIVATE flights performed in 2020 are shown in Figure 2. All flights originate from Langley, Virginia, going out as far east as ~67°W, as far south as ~32°N, and as far north as ~40°N. Table S1 in Supporting Information S1 summarizes the takeoff and landing times of each flight pictured in Figure 2, also summarizing the HSRL-2 mixed layer heights and RSP cloud fractions from each flight. MHLs range from 177 to 1906 m during the winter deployment and from 137 to 1775 m in the summer deployment. Cloud fractions range from 0% to 100% in both deployments.

Box plots of level leg mean wind speed, potential temperature  $\theta$ , and specific humidity  $q$  are given in Figure 3. Mean and median winter cloudy ensemble wind speeds are roughly the same at all level legs at ACB and below cloud (~9 m s<sup>-1</sup> means and ~8 m s<sup>-1</sup> medians) with higher spread wind speeds at BCT and ACT (11 and 12 m s<sup>-1</sup> means, respectively, and 10 m s<sup>-1</sup> medians). Interquartile ranges (IQRs, i.e., the difference between the 75th and 25th percentiles) are highest at ACT (18 m s<sup>-1</sup> vs. 8–12 m s<sup>-1</sup> below) (Figure 3a). Mean and median potential temperatures as well as IQRs are nearly constant at ~284 and ~12 K, respectively, up to the BCT typical of a mixed layer that is not decoupled (Figure 3b). Specific humidity profiles are what would be expected from a CTBL with a slight decrease through the cloud and a sharper decrease at ACT (Figure 3c).

Summer deployment cloudy ensemble wind profiles are very similar to those from the winter deployment (Figure 3d). Mixed layer potential temperatures are ~12 K warmer than in the winter deployment (Figure 3e). Specific humidity is also higher (Figure 3f). Wind speeds in the clear ensembles during the summer deployment are even lower than in the cloudy ensembles (Figures 3e and 3g). However, the potential temperature within the boundary layer in the summertime is similar in the clear or cloudy ensembles (Figure 3h). Also, the potential temperature at ABL in the clear ensembles is similar to that at ACT in the cloudy ensembles. Specific humidity

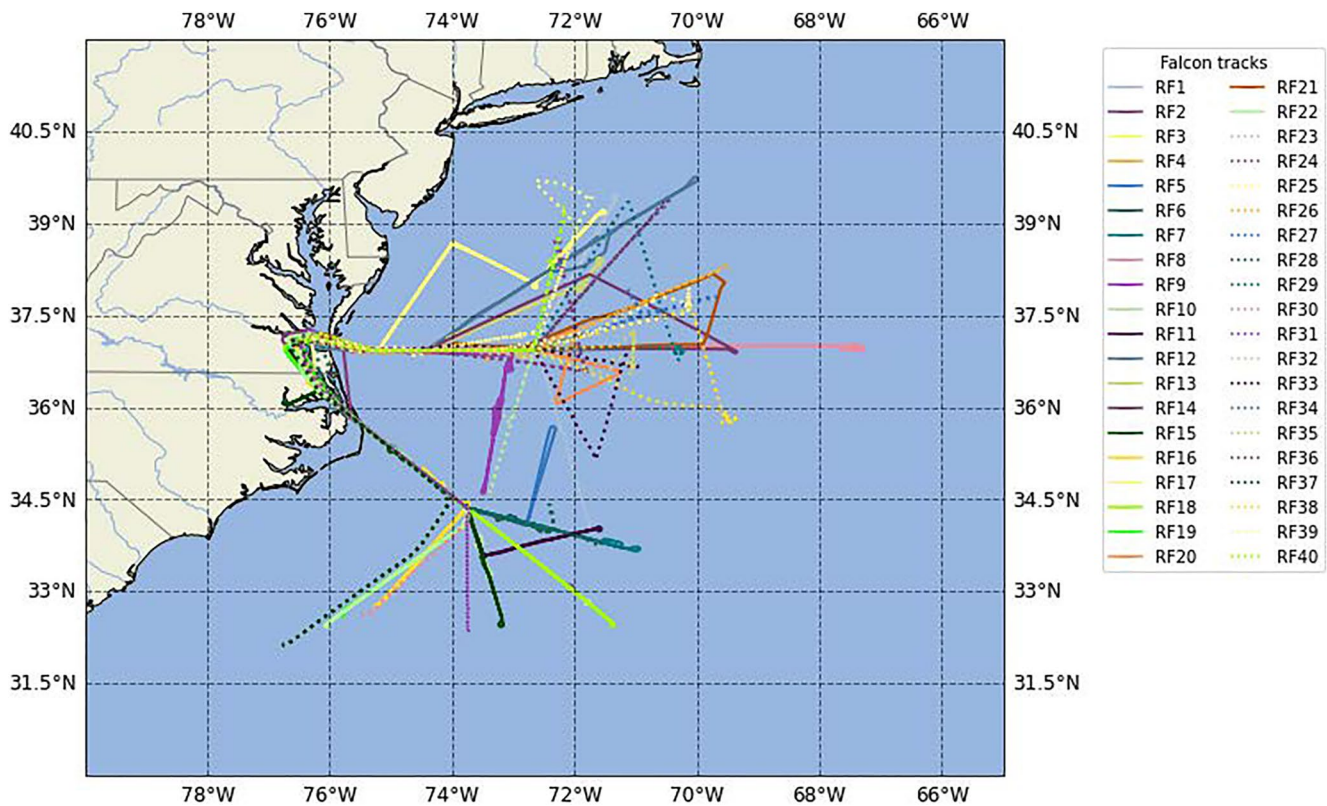


**Figure 2.** Flight tracks of the 2020 aerosol cloud meteorology interactions over the western Atlantic experiment flights. Winter deployment flights are shown in the solid lines, while the summer deployment flights are shown in the dotted lines.

in summer is also similar in the clear or cloudy ensembles, but there is a clear decrease in specific humidity from MinAlt up to ABL in the clear ensembles (Figure 3i).

In summary, during the 2020 deployment, wind speeds are nearly constant with height within the boundary layer but are highest in the winter cloudy ensembles. Potential temperatures and specific humidity are higher in summer than in winter. However, there is a distinct difference between humidity profiles in cloudy and clear ensembles, with nearly constant specific humidity within the boundary layer and decreasing specific humidity with height throughout the boundary layer, respectively. Another distinction between winter and summer conditions is that MLHs are slightly higher in winter. Next, we will summarize the observations of turbulent quantities made during the 2020 deployment.

#### 4.2. Turbulence Measurements

The frequency distributions of TKE for the cloudy ensembles are given in Figure 4. The distributions are wider, with frequency peaking at higher TKE within the boundary layer in winter (BCT and below, Figures 4b–4e). The median, mean, and IQRs are shown in Figure 5a and listed in Table 1. The highest median (mean) and IQR are 1.39 (1.71) and 1.20  $\text{m}^2 \text{s}^{-2}$ , respectively, at BCT. The lowest median (mean) TKE is 0.58 (0.70  $\text{m}^2 \text{s}^{-2}$ ) at ACT. Within the boundary layer, the lowest median (mean) and IQR (0.94/1.08 and 0.55  $\text{m}^2 \text{s}^{-2}$ ) are found at BCB.

Similar to TKE, the highest median (mean) and IQR in  $\langle u'^2 \rangle$  also occur at BCT: 1.91 (2.60) and 1.85  $\text{m}^2 \text{s}^{-2}$ , respectively (Figures 5b and Table 1). For  $\langle v'^2 \rangle$ , the highest median is at ACT (0.64  $\text{m}^2 \text{s}^{-2}$ ) (Figures 5c and Table 1), whereas it is highest at MinAlt (0.61  $\text{m}^2 \text{s}^{-2}$ ) in  $\langle w'^2 \rangle$  (Figures 5d and Table 1). Below ACT, mean and median  $\langle u'^2 \rangle$  is much higher than for  $\langle v'^2 \rangle$  and  $\langle w'^2 \rangle$  (Table 1). The similarity between TKE and  $\langle u'^2 \rangle$  suggests that most of TKE is going into zonal wind perturbations rather than in meridional or vertical wind perturbations. The near-surface peak in  $\langle w'^2 \rangle$  differs from what Dodson and Small Griswold (2021) found for subtropical stratocumulus.

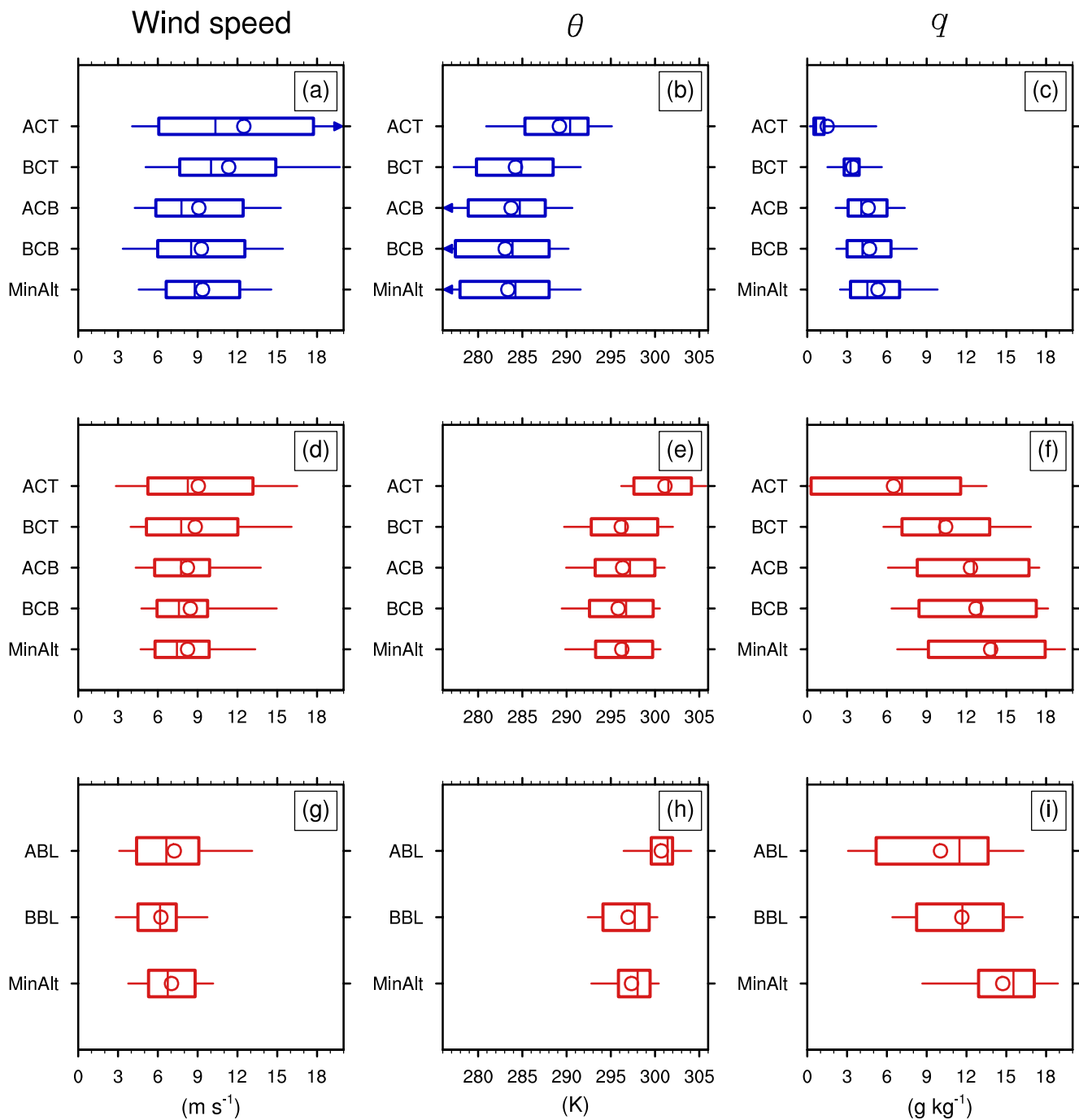


**Figure 3.** Box plots of wind speed, potential temperature, and specific humidity for winter cloudy (top row), summer cloudy (middle row), and summer clear (bottom row) modules. The boxes indicate the interquartile ranges from the 25th to 75th percentiles, and the vertical lines inside the boxes indicate the median values. The wings of the boxes span from the 10th to 90th percentiles. Arrows indicate that the wing extends beyond the edge of the plot. Also plotted are the mean values (open circles).

Turbulence in the summer deployment CTBL is lower in magnitude than those in the winter deployment as indicated by the lower median (mean) TKE for all level legs in Figure 5e. Frequency distributions are also narrower (Figure 4), as indicated by the generally smaller IQRs (Figures 5e and Table 1). Median (mean) TKE is highest at BCT ( $0.95 \text{ m}^2 \text{ s}^{-2}$  median and  $0.98 \text{ m}^2 \text{ s}^{-2}$  mean) as it is in winter. It similarly follows that the frequency distributions of the contributions to TKE (i.e.,  $\langle u'^2 \rangle$ ,  $\langle v'^2 \rangle$ , and  $\langle w'^2 \rangle$ ) in the summer deployment are narrower with medians that are lower than in the winter deployment (Figures 5f–5h).

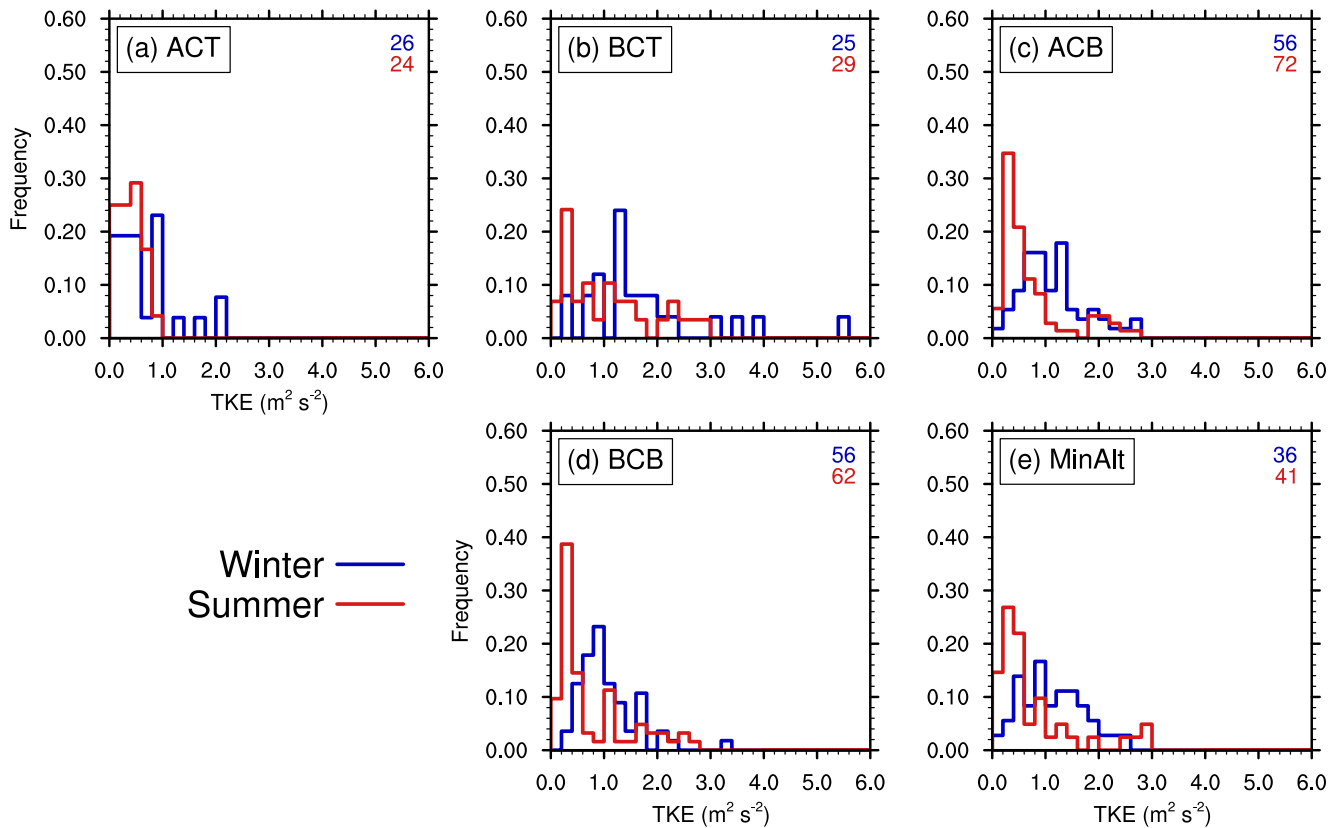


**Figure 4.** Frequency distributions of turbulence kinetic energy in cloudy ensembles during the winter (February and March 2020) and summer (August and September 2020) flights. The numbers in the upper right of each panel indicate the number of level legs.

Median TKE for summer deployment clear ensembles is smaller than for cloudy ensembles (Figures 5i and Table 1), and the frequency distributions are even narrower (Figure 6) as indicated by the smaller IQRs in Figure 5i. Median (mean) TKE ranges from 0.17 (0.23)  $\text{m}^2 \text{s}^{-2}$  at BBL to 0.34 (0.70)  $\text{m}^2 \text{s}^{-2}$  at MinAlt (Table 1). The wind variances contributing to TKE are also smaller (Figures 5j–5l & Table 1). Thus, clear boundary layers are less turbulent than cloudy ones, at least in summer, as clouds generally enhance boundary layer turbulence through cloud top radiative and evaporative cooling and cloud-bottom warming from condensation (Dodson & Small Griswold, 2021; Pasquier & Jonas, 1998).

The legs in the cloudy ensembles include both cloudy and clear portions. The cloud fraction derived from the cloud flags in the HSRL-2 measurements on board the King Air ranges from 0% to 100%. On average, though, the cloud fraction is higher in the winter deployment (41%) than in the summer (32%). Therefore, most cloudy ensemble legs are not completely cloud-covered. Crosbie et al. (2016) investigated the difference in turbulence across the boundaries between cloud and clearings in stratocumulus off of the California coast. They found that TKE in the clear air was lower than within the cloud. We also look at how the turbulence differs between the cloudy and clear portions of in-cloud legs ACB and BCT. Cloudy portions defined are samples in which liquid water content  $>0.2 \text{ g m}^{-3}$ . The frequencies in TKE and the wind variances in the clear portions peak at the same or lower values than in the cloudy portions in the winter ensembles (Figure S4 in Supporting Information S1). For instance, at BCT, TKE frequencies are highest at  $1.3 \text{ m}^2 \text{s}^{-2}$  for the cloudy portions, whereas they are highest at  $0.7 \text{ m}^2 \text{s}^{-2}$  for clear portions. However, the cloudy and clear frequency distributions are very similar in the summer ensembles (Figure S5 in Supporting Information S1).

Figure 7 and Table 2 present the medians, means, and IQRs for buoyancy fluxes  $F_b$  (Equation 6) and moisture fluxes  $F_q$  (Equation 7), the frequency distributions of which are shown in Figures S6 and S7 in Supporting Information S1. Median  $F_b$  is highest ( $46 \text{ W m}^{-2}$ ) at MinAlt and near-zero at the other legs above. Similarly, in the summer deployment cloudy ensembles, median  $F_b$  is highest at MinAlt but is much smaller in magnitude ( $7 \text{ W m}^{-2}$ ), and it is near-zero at the other legs above. Median  $F_b$  is near-zero at all levels in the summer deployment

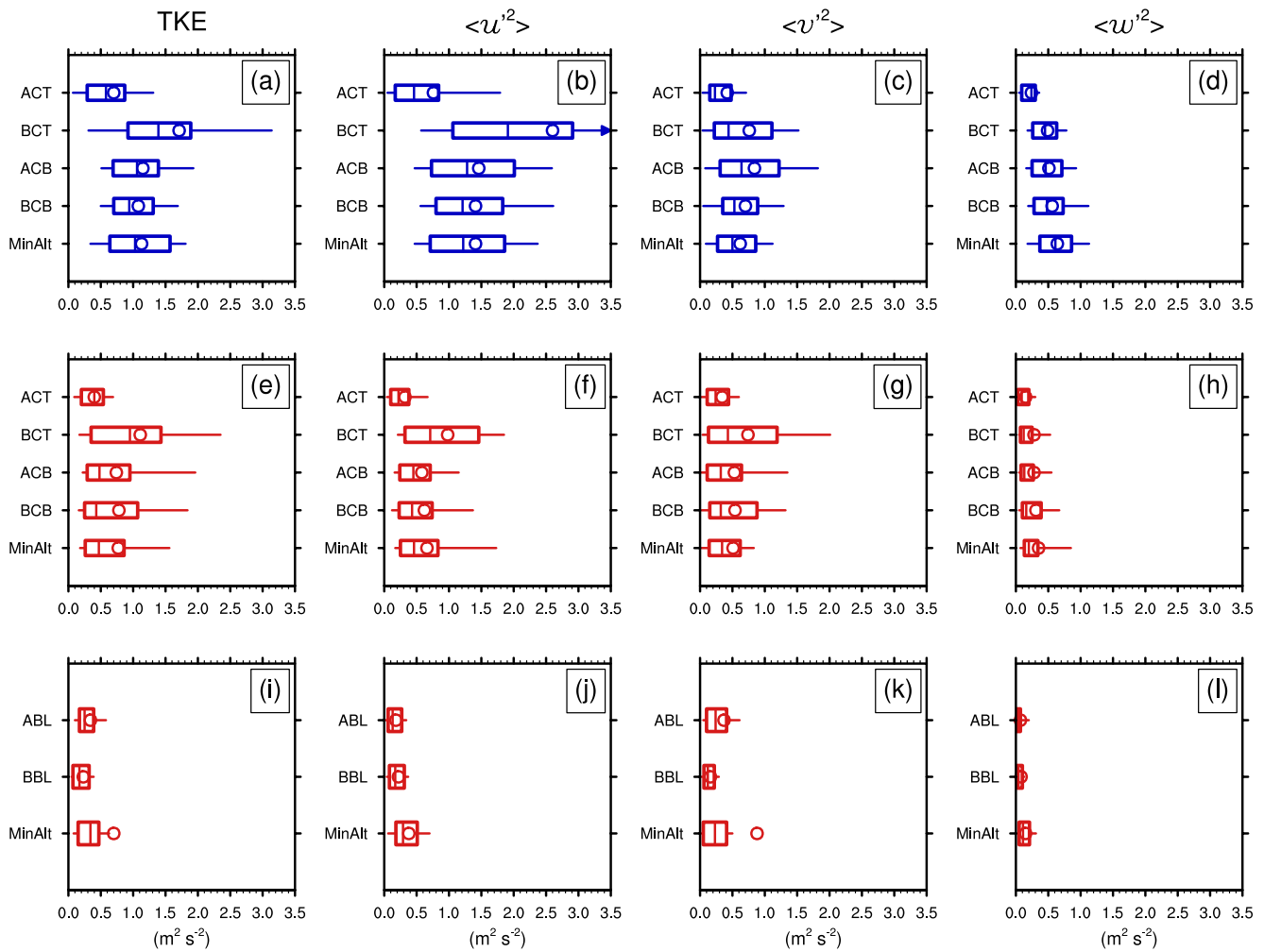


**Figure 5.** Box plots of turbulence kinetic energy and the horizontal and vertical wind variances in the winter cloudy (top), summer cloudy (middle), and summer clear ensembles (bottom). The boxes indicate the interquartile ranges from the 25th to 75th percentiles, and the vertical lines inside the boxes indicate the median values. The wings of the boxes span from the 10th to 90th percentiles. Arrows indicate that the wing extends beyond the edge of the plot. Also plotted are the mean values (open circles).

clear ensembles when the boundary layer winds are the weakest (Figure 3). In all three ensemble types, the highest mean  $F_b$  is at MinAlt. MinAlt is also the level with the highest  $\langle w'^2 \rangle$ , whereas the highest  $\langle u'^2 \rangle$  is at BCT, where there is higher wind shear (Figure 5). Therefore, below-cloud is more likely to be driven by surface-generated buoyancy, while the cloud layer is more influenced by wind shear.

Median  $F_q$  is greater below clouds (at BCB and MinAlt) than within clouds (at ACB and BCT), and is near-zero at ACT in winter and summer cloudy ensembles (Figure 7 & Table 2). This is to be expected, since there is a loss of water vapor from condensation in the cloud. The  $F_q$  values are generally greater in winter than in summer. In summer deployment clear ensembles, the median  $F_q$  is overall smaller.  $F_q$  can be negative from time to time. Many of these instances occur in downdrafts. Total water content  $q_t$  is a conservative quantity with the presence of clouds. Therefore,  $F_{q_t}$  should be continuously and linearly decreasing from below-to above-cloud (Garratt, 1992), but, in Figure 7 and Table 2,  $F_{q_t}$  is simply higher than  $F_q$ .

Median and mean vertical velocity skewness  $Sk_w$  derived from Equation 2 is near-zero at all levels and for all cloudy ensembles and clear ensembles during the summer deployment. This is consistent with the near-zero median  $\langle w'^3 \rangle$  (Figure 8, Table 3, Figures S8 and S9 in Supporting Information S1). In both winter and summer deployment cloudy ensembles,  $Sk_w$  is positive below cloud (at BCB and MinAlt) and at BCT but near-zero at ACB. The small  $Sk_w$  contrasts with the high  $Sk_w$  found in the mixed layer of a decoupled boundary layer in eastern

**Table 1**  
Median, Mean, and Interquartile Ranges of Turbulence Kinetic Energy (TKE) and Wind Variances ( $m^2 s^{-2}$ )

	Median			Mean			Interquartile range					
	$\overline{u'^2}$	$\overline{v'^2}$	$\overline{w'^2}$	TKE	$\overline{u'^2}$	$\overline{v'^2}$	$\overline{w'^2}$	TKE	$\overline{u'^2}$	$\overline{v'^2}$	$\overline{w'^2}$	
Winter cloudy ensembles												
ACT	0.58	0.46	0.23	0.24	0.70	0.76	0.42	0.24	0.58	0.67	0.33	0.21
BCT	1.39	1.91	0.44	0.45	1.71	2.60	0.76	0.49	0.97	1.85	0.89	0.37
ACB	1.06	1.28	0.64	0.46	1.15	1.46	0.84	0.51	0.70	1.28	0.91	0.46
BCB	0.94	1.21	0.53	0.48	1.08	1.41	0.70	0.56	0.61	1.03	0.54	0.45
MinAlt	1.03	1.22	0.50	0.61	1.13	1.41	0.62	0.64	0.93	1.15	0.59	0.49
Summer cloudy ensembles												
ACT	0.40	0.22	0.24	0.09	0.40	0.32	0.34	0.15	0.34	0.28	0.33	0.17
BCT	0.95	0.71	0.43	0.12	1.11	0.98	0.74	0.28	1.08	1.14	1.06	0.18
ACB	0.48	0.45	0.32	0.13	0.74	0.58	0.53	0.28	0.66	0.47	0.53	0.19
BCB	0.43	0.43	0.32	0.16	0.78	0.62	0.54	0.31	0.82	0.51	0.73	0.29
MinAlt	0.47	0.46	0.34	0.20	0.77	0.66	0.51	0.35	0.60	0.58	0.48	0.21
Summer clear ensembles												
ABL	0.25	0.13	0.24	0.04	0.34	0.18	0.37	0.07	0.22	0.21	0.31	0.06
BBL	0.17	0.17	0.12	0.04	0.23	0.22	0.16	0.08	0.25	0.23	0.16	0.08
MinAlt	0.34	0.29	0.23	0.11	0.70	0.38	0.88	0.15	0.32	0.33	0.36	0.16

North Atlantic stratocumulus (Lambert et al., 1999). According to Golaz et al. (2002), a positive  $Sk_w$  is indicative of cumulus cloud layers, which is the dominant cloud type in this region (Painemal et al., 2021). These observations indicate that positive  $Sk_w$  in cumulus-topped boundary layers exists below-cloud and near cloud top.

In summary, cloudy ensemble TKE reaches its maximum at BCT, with more TKE possible in the winter deployment than in the summer deployment. TKE is smallest in the summer clear ensembles.  $F_b$  in the cloudy ensembles is highest at MinAlt, higher in winter than in summer, but near-zero above. It is also near-zero on average at all levels during the summer clear ensembles.  $F_q$  is higher below cloud.  $Sk_w$  is near-zero at all levels.

### 4.3. Implications for Model Evaluation and Improvement

The ACTIVATE turbulence observations can be used to evaluate ESM simulated turbulence over the WNAO. For instance, boundary layer heights produced by CAM6 are consistent with the observed MLHs (173–2970 m during

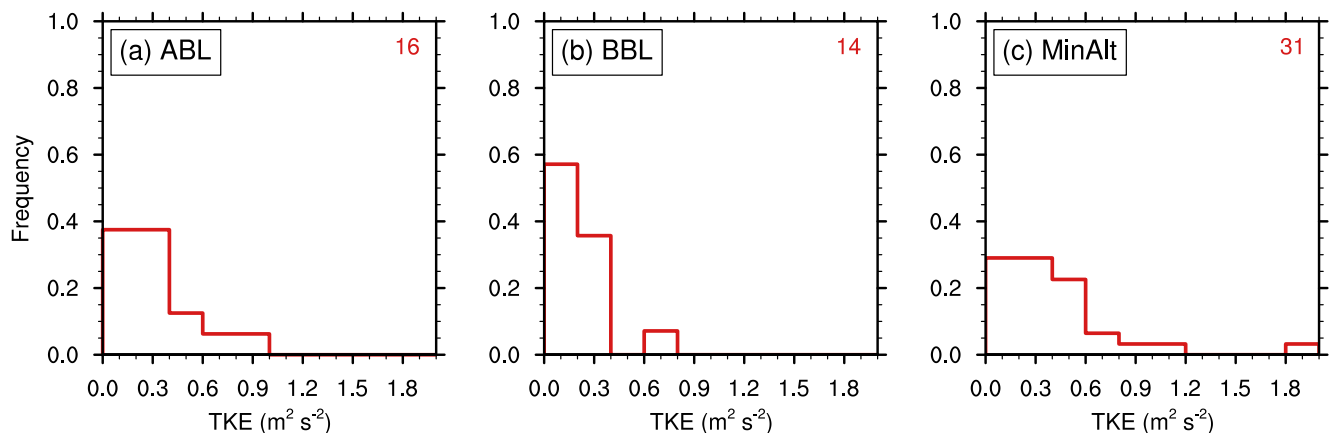


**Figure 6.** Frequency distributions of turbulent kinetic energy for the clear ensembles during the summer flights. The number given in each panel is the total number of samples used.

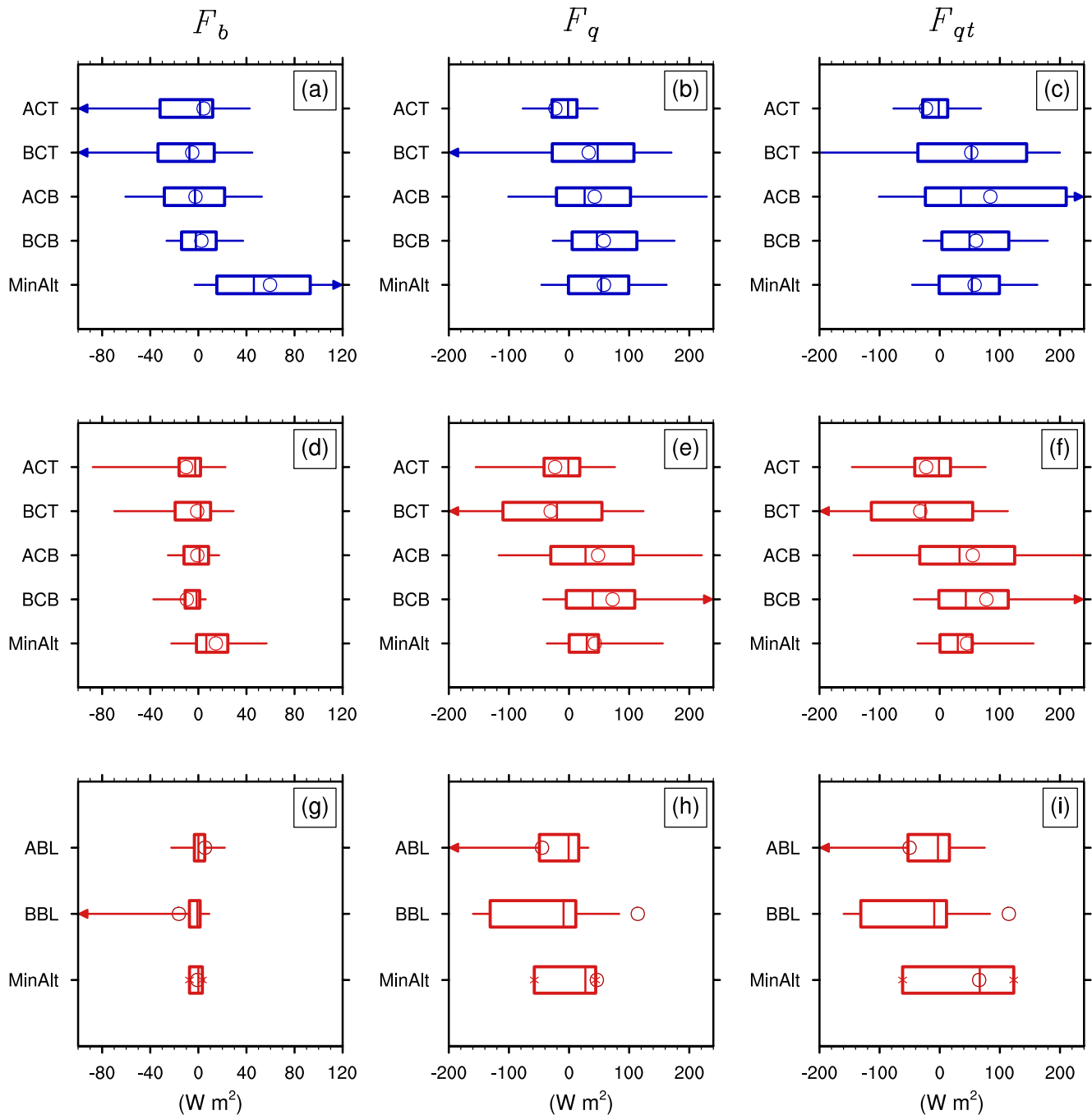


**Figure 7.** Box plots of buoyancy flux ( $F_b$ ), water vapor flux ( $F_q$ ), and total water flux ( $F_{qt}$ ) in the winter cloudy (top), summer cloudy (middle), and summer clear ensembles (bottom). The boxes indicate the interquartile ranges from the 25th to 75th percentiles, and the vertical lines inside the boxes indicate the median values. The wings of the boxes span from the 10th to 90th percentiles. Arrows indicate that the wing extends beyond the edge of the plot. Also plotted are the mean values (open circles). Note that there are different ranges in the x-axis in the various panels.

the CAM6 winter simulations vs. 177–1906 m from HSRL-2 and 181–1825 m during the summer simulations compared to 137–1775 m from HSRL-2). Further, we compare the observed vertical profiles of wind speed, potential temperature, and specific humidity from the nonlevel, cloudy legs of the aircraft to the vertical profiles in CAM6 (Figure 9). As indicated by the winter cloudy level legs, wind speeds during winter cloudy nonlevel legs on average are fairly constant up to  $\sim 1,600$  m, but there is a local maximum in average wind speed at  $\sim 200$  m. Average potential temperature vertical profiles are also nearly constant at  $\sim 282$  K to about  $\sim 1,200$  m. Average

**Table 2**  
*Median, Mean, and Interquartile Ranges of Buoyancy; Water Vapor and Total Water Fluxes ( $W m^{-2}$ )*

	Median			Mean			Interquartile range		
	$F_b$	$F_q$	$F_{qt}$	$F_b$	$F_q$	$F_{qt}$	$F_b$	$F_q$	$F_{qt}$
Winter cloudy ensembles									
ACT	1.39	-1.66	-1.66	4.39	-27.70	-22.88	43.78	41.55	41.55
BCT	-7.44	47.65	52.83	-7.44	32.72	52.42	46.78	135.84	180.85
ACB	-2.82	25.90	35.24	-2.82	42.63	84.21	50.10	123.14	234.28
BCB	-2.06	46.37	49.51	-2.06	57.80	60.28	28.84	107.67	111.26
MinAlt	46.17	53.39	53.39	59.60	58.06	58.07	77.68	100.25	100.26
Summer cloudy ensembles									
ACT	-2.63	-1.18	-1.18	-10.23	-23.18	-22.63	17.82	59.41	59.41
BCT	1.91	-20.09	-23.98	-0.97	-30.56	-32.41	29.47	188.89	168.55
ACB	1.01	27.40	32.93	-0.80	48.3	54.92	20.40	124.91	157.87
BCB	-1.49	39.38	43.39	-9.62	72.41	43.39	12.13	104.70	115.41
MinAlt	6.60	29.54	30.05	14.53	42.87	45.45	26.08	49.21	53.51
Summer clear ensembles									
ABL	0.04	-0.70	-2.96	3.14	-26.24	5.56	5.43	44.63	68.88
BBL	-0.83	-9.14	-9.14	4.34	-23.25	-16.19	8.20	113.73	142.53
MinAlt	0.01	27.17	66.57	5.60	39.10	-0.71	4.80	42.49	184.86

specific humidity profiles decrease with height from  $\sim 5 \text{ g kg}^{-1}$  near surface. Summertime cloudy average wind speed profiles are calmer than in winter but is also nearly constant up to a higher altitude. However, average potential temperatures and specific humidity are higher than in winter.

The average profiles from all ocean grid cells containing clouds in the ACTIVATE region from CAM6 is also shown in Figure 9. The winter (15 February–5 March) profiles of wind speed, potential temperature, and specific humidity are all within the observed spread (minimum to maximum) (Figures 9a–9c), but there are differences in the average profiles. Average profiles in wind speeds are in general higher than the observed averages (Figure 9a). Average potential temperature profiles are very similar to the observed average (Figure 9b), whereas specific humidity is a little higher than observed (Figure 9c).

CAM6 average wind speeds are smaller than the observed profile for summertime cloudy conditions (Figure 9d), but average potential temperature and specific humidity profiles are similarly biased in summer as in winter (Figures 9e and 9f). Still, average profiles for all three variables are generally within the observed spread.

The model spread is also shown as the area between the red-dashed lines. The observed spread is wider than observed in winter because the model simulations capture more variability in meteorological conditions than was sampled by the aircraft. However, in summer, the model spread is similar to the observed one, indicative of the persistence of similar conditions between the model simulations and the real world during the summer.

We also compare the observed vertical profiles of TKE and the contributions to TKE to the simulated ones in Figure 10. Observed average TKE for winter cloudy ensembles is  $\sim 0 \text{ m}^2 \text{ s}^{-2}$  up to  $\sim 825 \text{ m}$ , reaches a maximum at  $\sim 900 \text{ m}$ , and decreases back to  $\sim 0$  at  $\sim 1,600 \text{ m}$  (Figure 10a). Observational spread in TKE is also maximum at  $\sim 900 \text{ m}$ . Of the contributions to TKE, the vertical profile of  $\langle u'^2 \rangle$  is the most similar to that of TKE, whereas the averages and spread in  $\langle v'^2 \rangle$  and  $\langle w'^2 \rangle$  are much smaller (Figures 10b–10d). In CAM6, highest TKE is generated near the surface, so that model TKE is of course higher than observed (Figure 10a). Of the wind variances,  $\langle w'^2 \rangle$  is highest closer to the surface, whereas  $\langle u'^2 \rangle$  and  $\langle v'^2 \rangle$  are comparable to  $\langle w'^2 \rangle$  further up (Figures 10b–10d). In summertime cloudy ensembles, the average maximum TKE is at  $\sim 700 \text{ m}$  where the spread is also the maximum (Figure 10e). During these ensembles,  $\langle v'^2 \rangle$  vertical profiles are most similar to the TKE vertical profile (Figure 10g). CAM6 produces less TKE and smaller wind variances in summer (Figures 10e–10h). The difference between the observed horizontal wind variances indicates that the observed turbulence is not isotropic.

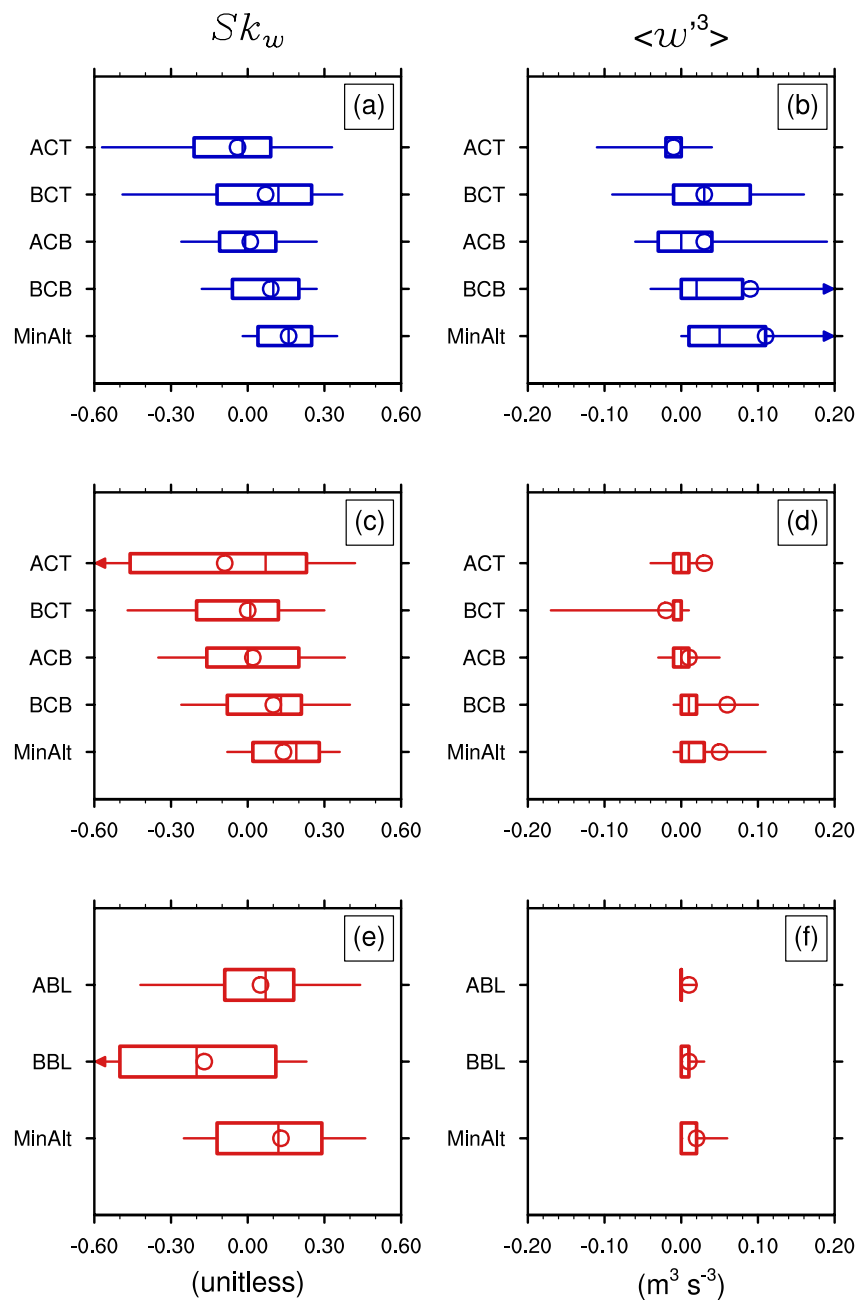


**Figure 8.** Box plots of vertical velocity skewness  $Sk_w$  and  $\langle w'^3 \rangle$  in the winter cloudy (top), summer cloudy (middle), and summer clear ensembles (bottom). The boxes indicate the interquartile ranges from the 25th to 75th percentiles, and the vertical lines inside the boxes indicate the median values. The wings of the boxes span from the 10th to 90th percentiles. Arrows indicate that the wing extends beyond the edge of the plot. Also plotted are the mean values (open circles).

We can further evaluate the simulated turbulence by comparing the observed frequency distributions of the wind variances to those produced by CLUBB in CAM6 and EAMv2. The observed frequency distributions for winter cloudy ensembles are shown in the top row of Figure 11. At ACT,  $\langle u'^2 \rangle$ ,  $\langle v'^2 \rangle$ , and  $\langle w'^2 \rangle$  are all most frequently at a low value  $<0.04 \text{ m}^2 \text{ s}^{-2}$  (Figure 11a). This remains the case for  $\langle v'^2 \rangle$  and  $\langle w'^2 \rangle$  at the lower level legs, but the frequency distribution in  $\langle u'^2 \rangle$  becomes wider at those level legs, indicating that  $\langle u'^2 \rangle$  is more often higher than  $\langle v'^2 \rangle$  and  $\langle w'^2 \rangle$  (Figures 11b–11e). This is consistent with the vertical profiles in Figure 10.

We can produce the same frequency distributions using all of the fully ocean grid cells in the ACTIVATE region ( $32^\circ\text{--}40^\circ\text{N}$  and  $67^\circ\text{--}77^\circ\text{W}$ ) containing cloud (liquid water content  $>0.2 \text{ g m}^{-3}$  anywhere in the model column

**Table 3**  
Median, Mean, and Interquartile Ranges of Skewness (Unitless) and the Moment of Vertical Velocity ( $m^3 s^{-3}$ )

	Median		Mean		Interquartile range	
	$Sk_w$	$\overline{w'^3}$	$Sk_w$	$\overline{w'^3}$	$Sk_w$	$\overline{w'^3}$
Winter cloudy ensembles						
ACT	-0.02	0	0.01	-0.01	0.30	0.02
BCT	0.12	0.03	-0.02	0.03	0.37	0.10
ACB	-0.01	0	0.003	0.03	0.22	0.07
BCB	0.1	0.02	-0.02	0.09	0.26	0.09
MinAlt	0.16	0.05	-0.04	0.11	0.21	0.10
Summer cloudy ensembles						
ACT	0.07	-0.01	-0.003	-0.01	0.69	0.02
BCT	0.01	0.03	0.004	0.03	0.32	0.01
ACB	0	0.03	0.001	0.03	0.36	0.02
BCB	0.13	0.09	-0.02	0.09	0.29	0.06
MinAlt	0.19	0.11	-0.04	0.11	0.26	0.03
Summer clear ensembles						
ABL	0.07	0.05	0.006	0.01	0.27	0
BBL	-0.20	-0.17	0.02	0.01	0.61	0.01
MinAlt	0.12	0.13	-0.02	0.02	0.41	0.02

where pressure >680 hPa). Because it is not really possible to define the same level legs in the model grids with coarse vertical and horizontal resolution, we generate frequency distributions for the layers that are in-cloud, below-cloud (but above the last model layer if the cloud does not go all the way down to that layer), and the lowest model layer (if the cloud does not go all the way down to this layer). These are shown for CAM6 in the middle row of Figure 11. CLUBB generates the lowest  $\langle u'^2 \rangle$  and  $\langle v'^2 \rangle$  most frequently in- and below-cloud and in the lowest model layer, whereas the frequency distribution in  $\langle w'^2 \rangle$  becomes wider below-cloud and in the lowest model layer, contrary to what is observed (Figures 11f–11h). Thus, the mean horizontal wind variances are lower than observed at all levels (e.g., 0.25–0.36  $m^2 s^{-2}$  for mean  $\langle u'^2 \rangle$  in CAM6 vs. 1.08–1.71  $m^2 s^{-2}$  mean observed in- or below-cloud) (Table 1 and Table S2 in Supporting Information S1). To see the effects that CLUBB parameter retuning would have, we also compare the EAMv2 vertical profiles to be observed. EAMv2's  $\langle w'^2 \rangle$  frequency distributions (bottom row) do not become as wide as in CAM6 below cloud in the lowest model layer. Therefore, the mean  $\langle w'^2 \rangle$  are lower than CAM6 at these two levels (Table S3 in Supporting Information S1).

Smaller mean wind variances and narrower distributions are produced in summer (Tables S3 and S5 and Figure S10 in Supporting Information S1). Therefore, despite the lesser turbulent boundary layers overall being produced in CAM6 and EAMv2, the model is simulating less turbulence in summer than in winter, as observed.

Furthermore, we can derive joint frequency distributions from the observations to assess the validity of the bivariate normal PDF over the WNAO. An example is given for vertical velocity perturbations  $w'$  and liquid potential

temperature perturbations  $\theta'_l$  in Figures 12a–12e for the cloudy ensembles in the winter deployment. The joint frequency distributions are consistent with a bivariate normal distribution at every level. The univariate distributions of the individual quantities  $w'$  and  $\theta'_l$  appear to be Gaussian with a near-zero skewness, consistent with Figure 8 & Table 3. The bivariate frequency distributions become wider along the  $w'$  axis going down toward the surface, as the  $w'$  distributions become wider with decreasing height (Figures 12f–12j) with standard deviations ranging from 0.60  $m^2 s^{-2}$  at ACT to 1.1  $m^2 s^{-2}$  at MinAlt. On the other hand, the  $\theta'_l$  distributions are similarly narrow at lower heights than at ACT (Figures 12k–12o). Similar distributions are found for the cloudy ensembles in the summer deployment (Figure S11 in Supporting Information S1), but they are less skewed at lower levels. For the clear summer deployment ensembles, the distributions are not skewed at any level (Figure S12 in Supporting Information S1).

On average, median TKE is highest at BCT, that is, within cloud, in the cloudy ensembles in both deployments, whereas model TKE is highest near-surface in Figure 10. Maximum TKE within cloud suggests that the CTBL is coupled, whereas maximum TKE below-cloud would be consistent with the cloud layer being decoupled from the surface mixed layer (Durand & Bourcy, 2001). This is further illustrated in six examples of instantaneous TKE vertical profiles in CAM6. Figure S13 in Supporting Information S1 gives three examples from the CAM6 winter simulations at a location near the middle of the ACTIVATE region (37°N and 72.5°W), while Figure S14 in Supporting Information S1 gives three examples from the summer simulations. On 24 February 2004, the model generates maximum TKE below cloud indicative of decoupling, whereas maximum TKE is near-surface on 24 February 2006 and 2008 with a secondary maximum of TKE at the cloud top in 2006. In summer, with the cloud cover on 27 August 2004, maximum TKE is generated at the cloud top, as on 24 August 2004 but is near-surface in the other summer examples with no cloud cover.

The model generates maximum TKE most often below cloud (72%) in the winter simulations, while it is generated 25% of instances in the lowest model layer and only 3% of the time within cloud. In summer, the model still generates maximum TKE most frequently below cloud (59%) but generates it more often in the lowest model layer (39%). The preponderance of decoupling in the model is contradicted by the ACTIVATE observations, with maximum TKE below cloud (at BCB) only 2% of the time in winter and 4% in summer. Instead, maximum TKE

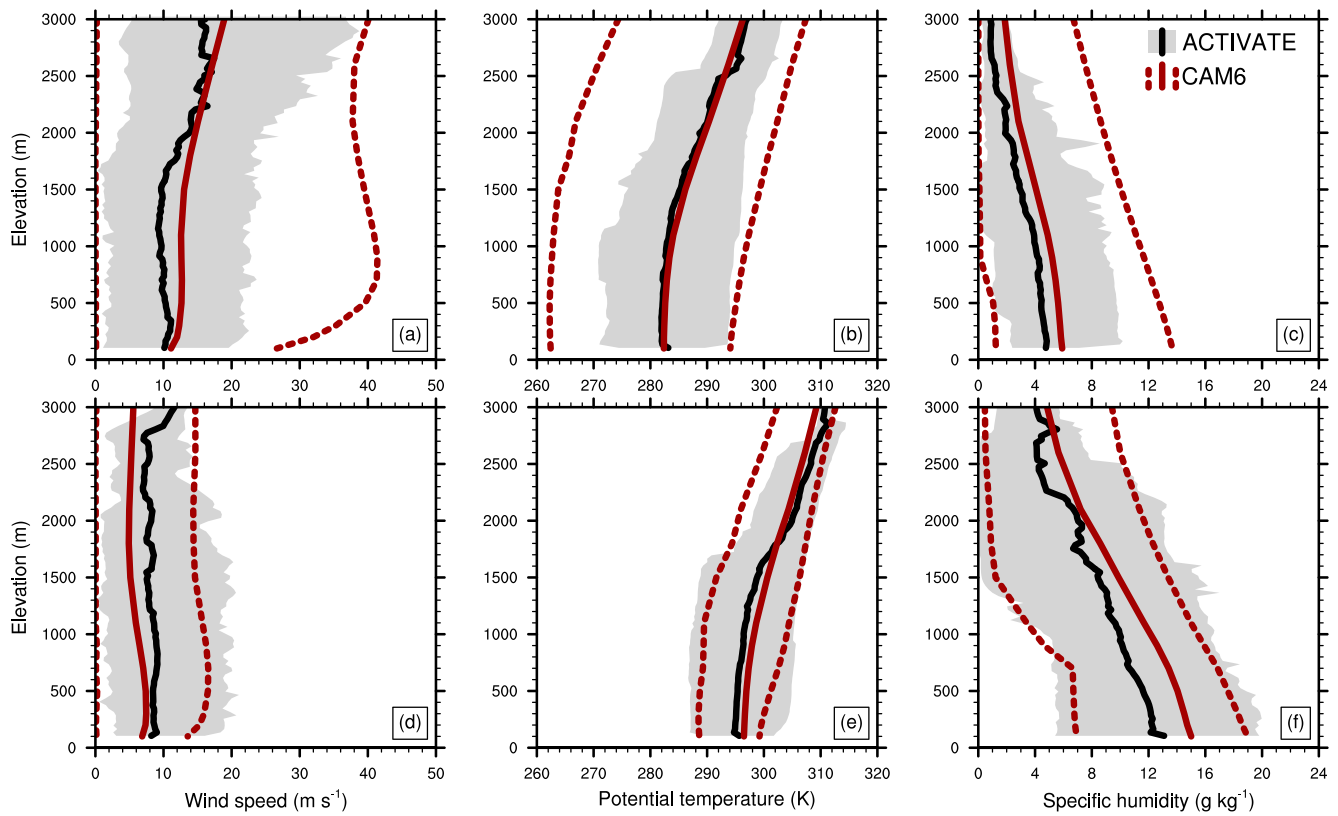


**Figure 9.** Mean vertical profiles of wind speed, potential temperature, and specific humidity for nonlevel legs during the winter (top) and summer (bottom) deployments. These are compared to the average vertical profiles from the cloud-containing grid cells in the community atmosphere model version 6 winter (top) and summer (bottom) simulations. The minimum to maximum range in the observations is indicated by the gray shading.

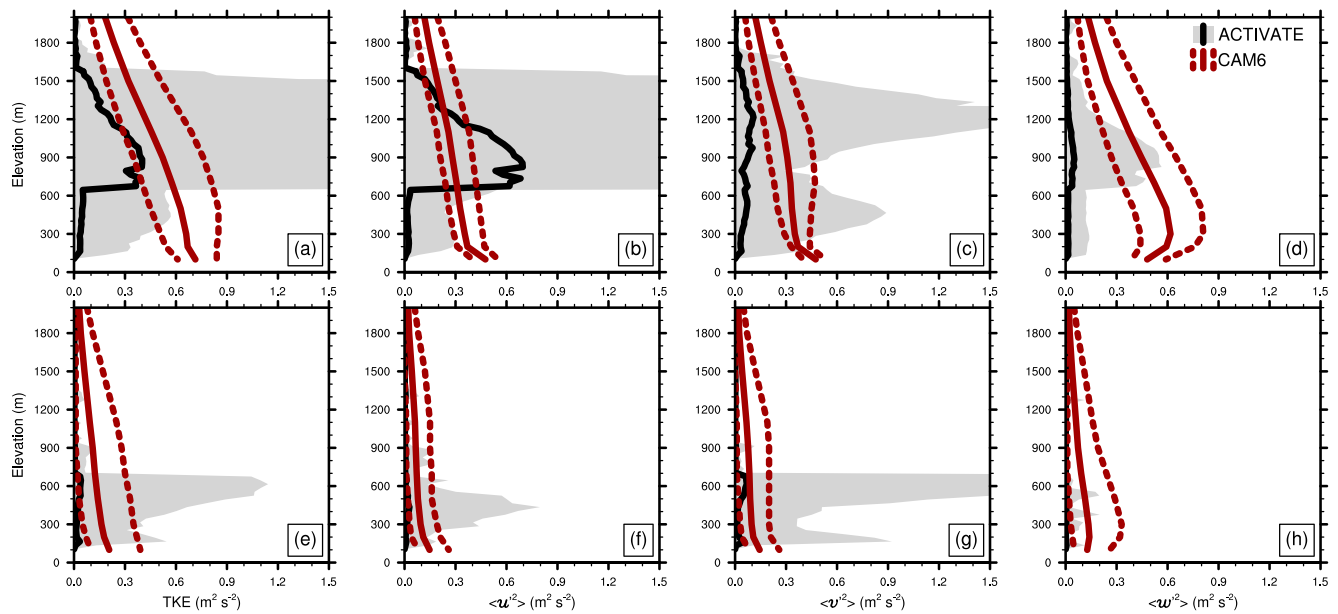


**Figure 10.** Mean vertical profiles of turbulence kinetic energy,  $\langle u'^2 \rangle$ ,  $\langle v'^2 \rangle$ , and  $\langle w'^2 \rangle$  for nonlevel legs during the winter (top) and summer (bottom) deployments. These are compared to the average profiles from the cloud-containing grid cells in the community atmosphere model version 6 winter (top) and summer (bottom) simulations. The minimum to maximum range in the observations is indicated by the gray shading. Note that some of that range extends outside the panel maximum of  $1.5 \text{ m}^2 \text{ s}^{-2}$ .

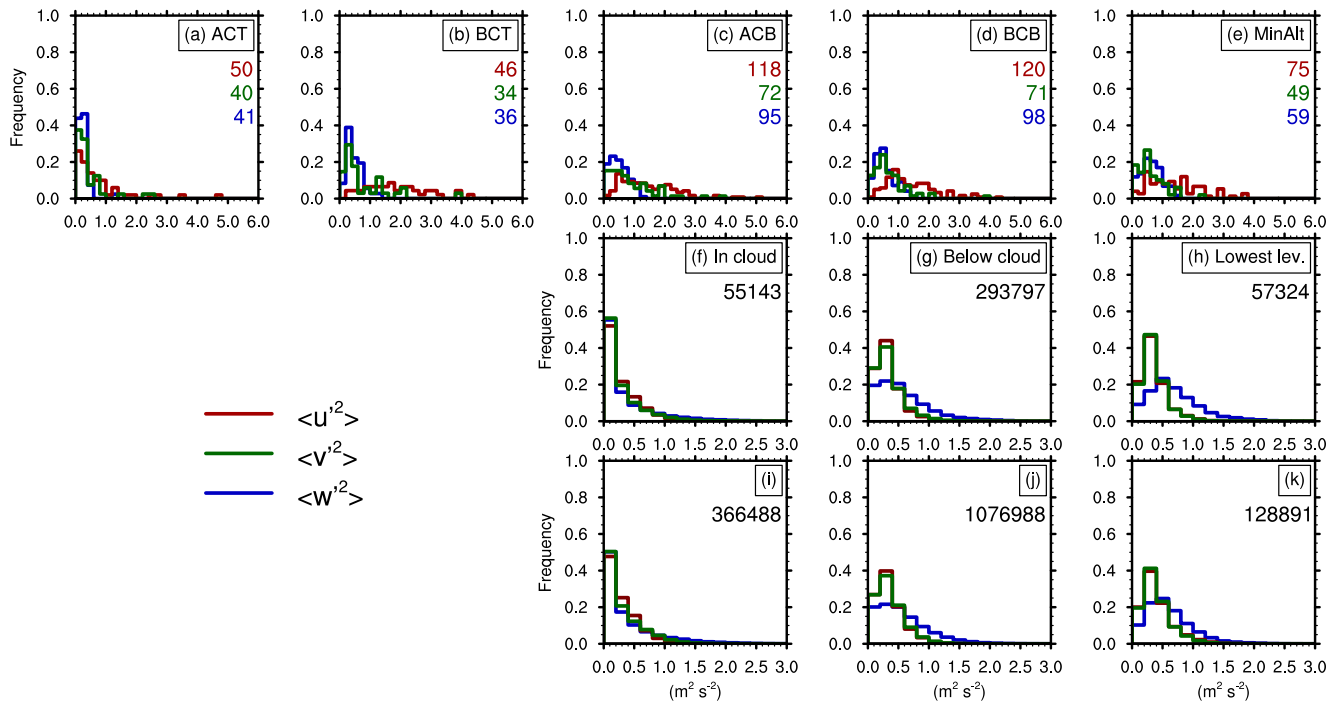


**Figure 11.** (a–e) Frequency distributions of  $\langle u'^2 \rangle$  (red),  $\langle v'^2 \rangle$  (green), and  $\langle w'^2 \rangle$  (blue) at each level leg in cloudy ensembles during the winter deployment. Also shown are the frequency distributions from cloudy grid cells in the (f–h) community atmosphere model version 6 and (i–k) atmosphere model version 2 winter simulations. The numbers given in each panel are the total number of samples used (for each quantity identified by matching colors in the observations in the top row). Note the difference in the x-axes.

is more often within cloud (at ACB or BCT; 36% in the winter deployment and 51% in the summer deployment), with it being at MinAlt 27% of the time in both deployments. This within-cloud maximum TKE has been shown to be common in CTBLs (e.g., Dodson & Small Griswold, 2020). Decoupling is often associated with precipitation. The predominance of model decoupling has been shown to be due to evaporation of precipitation below cloud (Zheng et al., 2020). During the 2020 deployments, the amount of precipitating 2DS samples is only 1% in the winter deployment and 0% in summer. With such little precipitation sampling in these two deployments, it is not possible to properly investigate the effects of precipitation on the observed turbulence here.

Even when the maximum TKE is below-cloud, a local TKE maximum may still exist in-cloud. To illustrate this, we use LES for the process study days of 28 February, 1 March, and 2 June 2020 for which domain average TKE profiles are shown in Figure 13. TKE is highest in-cloud on 28 February, while there is a local maximum in TKE on 1 March. Both the absolute and local maxima occur near the cloud top. There is also a small local maximum in TKE within the deeper cloud layer of 2 June. Higher or highest TKE in all three profiles can be found just above the surface, with a minimum in TKE just above cloud base. The above results are from the 300-m resolution LES. We tested the sensitivity of boundary layer structure and turbulence fluxes to the horizontal resolution in a simulation with a finer horizontal resolution of 100 m and found that the finer resolution LES yields essentially the same results as the coarser resolution. These LES results are consistent with the ACTIVATE observations (Figure S15 in Supporting Information S1).

Model horizontal wind variance may be lower because of the intrinsic difference between what is represented by the linear aircraft measurements and the coarse grid cells in the ESM. We test if this is possible by randomly sampling LES columns containing clouds that would be more representative of what would be seen by an aircraft. There is a wide variation in TKE in all simulations, from values lower than the domain average to values much larger (Figure 13).

While it might be natural to have lower mean TKE represented by the coarse grid cells in an ESM, the widest distributions are from  $\langle w'^2 \rangle$ , especially lower in the model vertical profile, whereas it is in  $\langle u'^2 \rangle$  in the observations (Figure 11). In the mean vertical profiles (Figure 10), highest TKE is generated near the surface. Of the wind variances,  $\langle w'^2 \rangle$  is highest closer to the surface, whereas  $\langle u'^2 \rangle$  and  $\langle v'^2 \rangle$  are higher than  $\langle w'^2 \rangle$  further

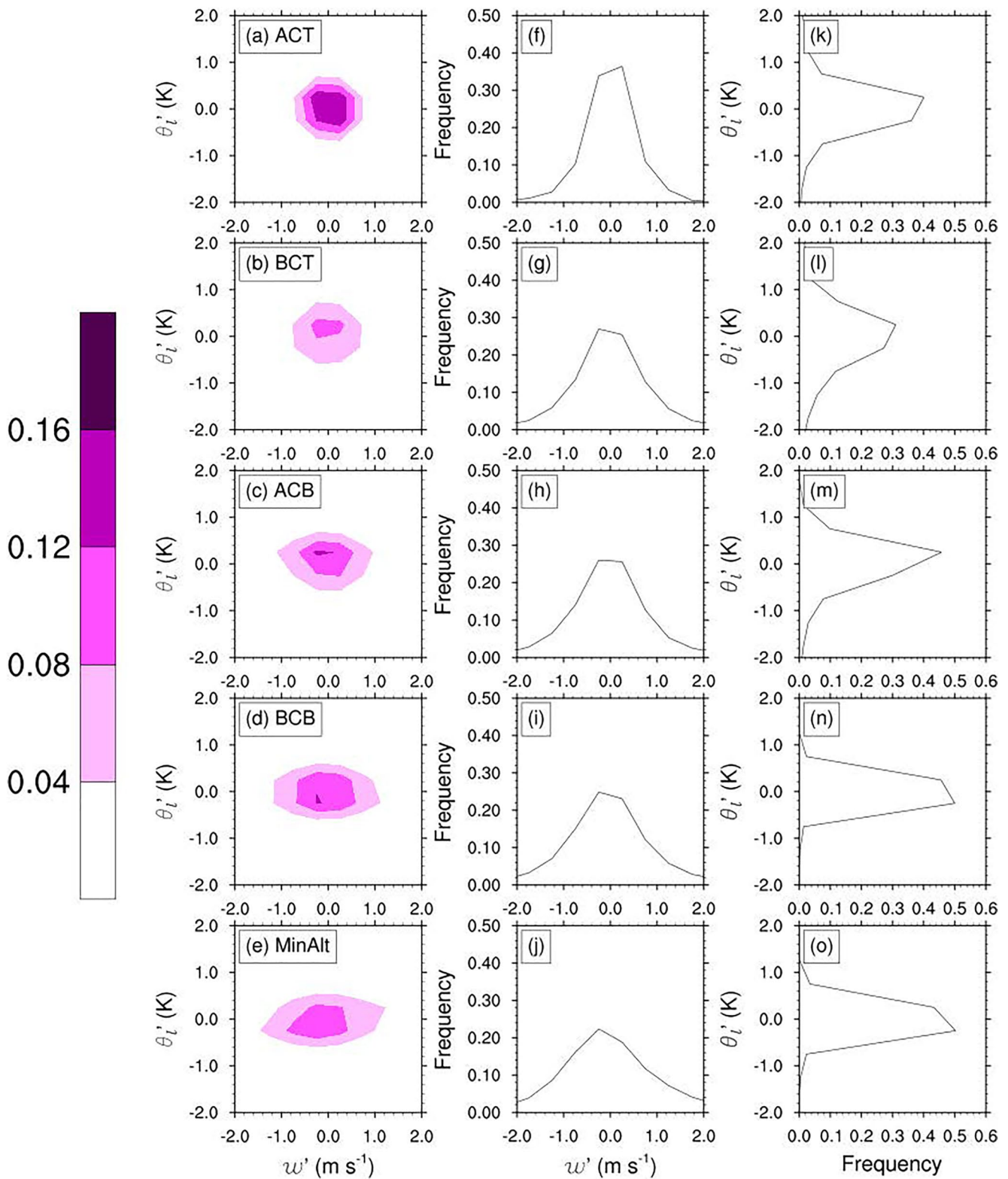


**Figure 12.** (a–e) Bivariate frequency distributions between observed turbulent perturbations in liquid potential temperature  $\theta'_l$  and vertical velocity  $w'$  and univariate distributions of (f–j)  $w'$  and (k–o)  $\theta'_l$  for each of the level legs in cloudy ensembles during the winter deployment.



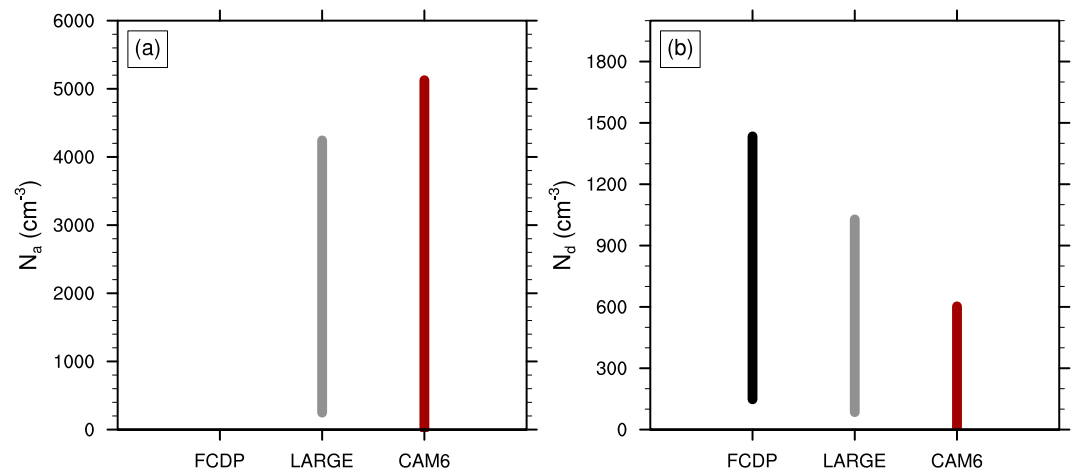


**Figure 14.** Ranges of (a) below cloud base cloud aerosol number concentration ( $N_a$ ) and (b) above cloud base cloud droplet number concentration ( $N_d$ ) from observations and from all of the 15-day simulations of enhanced output in community atmosphere model version 6 for the winter (19 February–5 March simulations).

The weaker turbulence coming from CLUBB as used in CAM6 might be rectified from a revision of its parameters. Ma et al. (2021) recently performed a retuning of the parameters used to define the width of the bivariate normal PDFs as well as the effects of the turbulence skewness  $Sk_w$  in the determination of quantities in the development of the E3SM EAMv2. This retuning was performed using theoretical considerations to improve the simulation of mostly subtropical stratocumulus decks. Only observations of bulk cloud properties (e.g., the top-of-atmosphere cloud radiative effects) were used in the retuning. To see the effect of these retuning on turbulence characteristics, we also performed similar simulations in EAMv2 for 2004–2010, as was done in CAM6. The velocity variance frequency distributions from these simulations were also compared to observations and those of CAM6. EAMv2's frequency distributions are closer to the observed ones, showing an improvement over CAM6 and more drastically from the pre-retuning version EAMv1 (not shown). However, the EAMv2 frequency distributions still represent less turbulent conditions than observed in CLUBB; the bivariate normal PDFs are not used to close the horizontal wind variances. Instead, these quantities are prognosed using equations that include a term that defines the dissipation of TKE in those directions using a prescribed parameter. Such a parameter may need to be further tuned in addition to the parameters that define the shape of the binormal PDFs by  $Sk_w$ . Using ACTIVATE measurements to constrain the tuning of the turbulence parameterization will be very helpful.

The EAMv2 and CAM6 turbulent quantities as well as the cloud and aerosol microphysical quantities presented here are the instantaneous output at the 30-min time steps. This represents the outcome of the iteration of several (six in EAMv2) substeps performed by CLUBB within each time step. On a global scale, the behavior of the turbulence and cloud microphysics parameterizations can show discernible differences across the different substeps (not shown). Whether such cross-substep variations are significant in the time periods and spatial domain covered by ACTIVATE is not yet clear and will be investigated further.

The results presented here demonstrate that the analysis of the full set of ACTIVATE turbulence observations can be used to aid in the revision of CLUBB in CAM6 and EAMv2 for the improvement of extratropical low-level clouds. The role of large-scale meteorological conditions can also be explored with the full set of observations by stratifying the observations by quantities like lower tropospheric stability or cold air outbreak index. The limited amount of observations in this first glance at the first two ACTIVATE deployments presents the motivation for such an analysis to be done rigorously in the near future.

### Data Availability Statement

The Aerosol Cloud Meteorology Interactions over the Western Atlantic Experiment data used in this study can be downloaded from the experiment's archive ([www-air.larc.nasa.gov/missions/activate/index.html](http://www-air.larc.nasa.gov/missions/activate/index.html); <https://doi.org/10.5067/SUBORBITAL/ACTIVATE/DATA001>, ACTIVATE, (2021)). Community Atmosphere Model version 6 and the Energy Exascale Earth System Model (E3SM) Atmosphere Model version 2 can be downloaded as part of the Community Earth System Model version 2 and E3SMv2. Details on downloading these Earth

system models can be found at [https://www.cesm.ucar.edu/models/cesm2/release\\_download.html](https://www.cesm.ucar.edu/models/cesm2/release_download.html) and <https://e3sm.org/v2-release-publicity>, respectively.

### Acknowledgments

The work was funded by NASA (Grant 80NSSC19K0442) in support of Aerosol Cloud Meteorology Interactions over the Western Atlantic Experiment, a NASA Earth Venture Suborbital-3 investigation funded by the NASA's Earth Science Division and managed through the Earth System Science Pathfinder Program Office. It was also supported by the DOE SciDAC Program (Grant 70276). The Pacific Northwest National Laboratory is operated for DOE by the Battelle Memorial Institute under contract DE-AC05-76RLO1830. Four anonymous reviewers are thanked for their helpful comments.

### References

- Abel, S. J., Boutle, I. A., Waite, K., Fox, S., Brown, P. R. A., Cotton, R., et al. (2017). The role of precipitation in controlling the transition from stratocumulus to cumulus clouds in a northern hemisphere cold-air outbreak. *Journal of the Atmospheric Sciences*, *74*(7), 2293–2314. <https://doi.org/10.1175/JAS-D-16-0362.1>
- Ackerman, A. S., Kirkpatrick, M. P., Stevens, D. E., & Toon, O. B. (2004). The impact of humidity above stratiform clouds on indirect aerosol climate forcing. *Nature*, *432*(7020), 1014–1017. <https://doi.org/10.1038/nature03174>
- ACTIVATE. (2021). ACTIVATE Campaign Preliminary Repository [Collection]. NASA/Langley Research Center. <https://doi.org/10.5067/SUBORBITAL/ACTIVATE/DATA001>
- Albrecht, B. A. (1989). Aerosols, cloud microphysics, and fractional cloudiness. *Science*, *245*(4923), 1227–1230. <https://doi.org/10.1126/science.245.4923.1227>
- Arakawa, A., & Schubert, W. H. (1974). Interaction of a cumulus cloud ensemble with the large-scale environment, Part I. *Journal of the Atmospheric Sciences*, *31*(3), 674–701. [https://doi.org/10.1175/1520-0469\(1974\)031<0674:ioacce>2.0.co;2](https://doi.org/10.1175/1520-0469(1974)031<0674:ioacce>2.0.co;2)
- Atkinson, B. W., & Zhang, J. W. (1996). Mesoscale shallow convection in the atmosphere. *Reviews of Geophysics*, *34*(4), 403–431. <https://doi.org/10.1029/96rg02623>
- Atlas, D., Chou, S. H., & Byerly, W. P. (1983). The influence of coastal shape on winter mesoscale air sea interaction. *Monthly Weather Review*, *111*(2), 245–252. [https://doi.org/10.1175/1520-0493\(1983\)111<0245:TIOCSO>2.0.CO;2](https://doi.org/10.1175/1520-0493(1983)111<0245:TIOCSO>2.0.CO;2)
- Atlas, R. L., Bretherton, C. S., Blossy, P. N., Gettelman, A., Bardeen, C., Lin, P., & Ming, Y. (2020). How well do large-eddy simulations and global climate models represent observed boundary layer structures and low clouds over the summertime Southern Ocean? *Journal of Advances in Modeling Earth Systems*, *12*(11), e2020MS002205. <https://doi.org/10.1029/2020MS002205>
- Bane, J., & Osgood, K. E. (1989). Wintertime air-sea interaction processes across the gulf-stream. *Journal of Geophysical Research*, *94*(C8), 10755–10772. <https://doi.org/10.1029/JC094iC08p10755>
- Boers, R., & Melfi, S. H. (1987). Cold-air outbreak during MASEX—Lidar observations and boundary-layer model test. *Boundary-Layer Meteorology*, *39*(1–2), 41–51. <https://doi.org/10.1007/bf00121864>
- Bogenschutz, P. A., & Krueger, S. K. (2012). A simplified PDF parameterization of subgrid-scale clouds and turbulence for cloud-resolving models. *Journal of Advances in Modeling Earth Systems*, *5*(2), 195–211. <https://doi.org/10.1002/jame.20018>
- Bony, S., Colman, R., Kattsov, V. M., Allan, R. P., Bretherton, C. S., Dufresne, J.-L., et al. (2006). How well do we understand and evaluate climate change feedback processes? *Journal of Climate*, *19*(15), 3445–3482. <https://doi.org/10.1175/jcli3819.1>
- Bony, S., & Dufresne, J.-L. (2005). Marine boundary layer clouds at the heart of tropical cloud feedback uncertainties in climate models. *Geophysical Research Letters*, *32*(20), L20806. <https://doi.org/10.1029/2005GL023851>
- Boucher, O., Randall, D., Artaxo, P., Bretherton, C., Feingold, G., Forster, P., et al. (2013). Clouds and aerosols. In T. F. Stocker, D. Qin, G.-K. Plattner, M. Tignor, S. K. Allen, J. Boschung, et al. (Eds.), *Climate change 2013: The physical science basis. Contribution of working group I to the fifth assessment report of the intergovernmental panel on climate change*. Cambridge University Press.
- Bretherton, C. S., & Park, S. (2009). A new moist turbulence parameterization in the community atmosphere model. *Journal of Climate*, *22*(12), 3422–3448. <https://doi.org/10.1175/2008JCLI2556.1>
- Brilouet, P.-E., Durand, P., Canut, G., & Fourrié, N. (2020). Organized turbulence in a cold-air outbreak: Evaluating a large-eddy simulation with respect to airborne measurements. *Boundary-Layer Meteorology*, *175*(1), 57–91. <https://doi.org/10.1007/s10546-019-00499-4>
- Brunke, M. A., de Szoeko, S. P., Zuidema, P., & Zeng, X. (2010). A comparison of ship and satellite measurements of cloud properties with global climate model simulations in the southeast Pacific stratus deck. *Atmospheric Chemistry and Physics*, *10*(14), 6527–6536. <https://doi.org/10.5194/acp-10-6527-2010>
- Calmer, R., Roberts, G. C., Preissler, J., Sanchez, K. J., Derrien, S., & O'Dowd, C. (2018). Vertical wind velocity measurements using a five-hole probe with remotely piloted aircraft to study aerosol-cloud interactions. *Atmospheric Measurement Techniques*, *11*(5), 2583–2599. <https://doi.org/10.5194/amt-11-2583-2018>
- Choi, Y.-S., Ho, C.-H., Kim, S.-W., & Lindzen, R. S. (2010). Observational diagnosis of cloud phase in the winter Antarctic atmosphere for parameterizations in climate models. *Advances in Atmospheric Sciences*, *27*(6), 1233–1245. <https://doi.org/10.1007/s00376-010-9175-3>
- Choi, Y.-S., Ho, C.-H., Park, C.-E., Storelvmo, T., & Tan, I. (2014). Influence of cloud phase composition on climate feedbacks. *Journal of Geophysical Research: Atmospheres*, *119*(7), 3687–3700. <https://doi.org/10.1002/2013JD020582>
- Conant, W. C., VanReken, T. M., Rissman, T. A., Varutbangkul, V., Jonsson, H. H., Nenes, A., et al. (2004). Aerosol-cloud drop concentration closure in warm cumulus. *Journal of Geophysical Research*, *109*(D13), D13204. <https://doi.org/10.1029/2003JD004324>
- Corral, A. F., Braun, R. A., Cairns, B., Gorrooh, V. A., Liu, H., Ma, L., et al. (2021). An overview of atmospheric features over the western north Atlantic ocean and north American East Coast—Part I: Analysis of aerosols, gases, and wet deposition chemistry. *Journal of Geophysical Research: Atmospheres*, *126*(4), e2020JD032592. <https://doi.org/10.1029/2020JD032592>
- Crosbie, E., Wang, Z., Sorooshian, A., Chuang, P. Y., Craven, J. S., Coggon, M. M., et al. (2016). Stratocumulus cloud clearings and notable thermodynamic and aerosol contrasts across the clear-cloudy interface. *Journal of the Atmospheric Sciences*, *73*(3), 1083–1099. <https://doi.org/10.1175/JAS-D-15-0137.1>
- Dadashazar, H., Painemal, D., Alipanah, M., Brunke, M., Chellappan, S., Corral, A. F., et al. (2021). Cloud drop number concentrations over the western north Atlantic ocean: Seasonal cycle, aerosol interrelationships, and other influential factors. *Atmospheric Chemistry and Physics*, *21*(13), 10499–10526. <https://doi.org/10.5194/acp-21-10499-2021>
- Danabasoglu, G., Lamarque, J.-F., Bacmeister, J., Bailey, D. A., DuVivier, A. K., Edwards, J., et al. (2020). The community Earth system model version 2 (CESM2). *Journal of Advances in Modeling Earth Systems*, *12*, e2019MS001916. <https://doi.org/10.1029/2019MS001916>
- de Roode, S. R., Sandu, I., van der Dussen, J. J., Ackerman, A. S., Blossy, P., Jarecka, D., et al. (2016). Large-eddy simulations of EUCLIPSE-GASS lagrangian stratocumulus-to-cumulus transitions: Mean state, turbulence, and decoupling. *Journal of the Atmospheric Sciences*, *73*(6), 2485–2508. <https://doi.org/10.1175/JAS-D-15-0215.1>
- D. H. Lenschow (Ed.) (1986). *Probing the atmospheric boundary layer*. American Meteorological Society.
- Dirks, R. A., Kuettner, J. P., & Moore, J. A. (1988). Genesis of Atlantic lows experiment (GALE)—An overview. *Bulletin of the American Meteorological Society*, *69*(2), 148–160. [https://doi.org/10.1175/1520-0477\(1988\)069<0148:goalea>2.0.co;2](https://doi.org/10.1175/1520-0477(1988)069<0148:goalea>2.0.co;2)

- Dodson, D. S., & Small Griswold, J. D. (2021). Turbulent and boundary layer characteristics during VOCALS-REx. *Atmospheric Chemistry and Physics*, 21(3), 1937–1961. <https://doi.org/10.5194/acp-21-1937-2021>
- Durand, P., & Bourcy, T. (2001). Observations of the turbulence structure within two stratocumulus-topped, marine boundary layers. *Boundary-Layer Meteorology*, 89(1), 105–125. <https://doi.org/10.1023/a:1018999221303>
- E3SM Project, DOE. (2021). Energy Exascale Earth system model v2.0 [Software]. Github. <https://doi.org/10.11578/E3SM/dc.20210927.1>
- Fountoukis, C., Nenes, A., Meskhidze, N., Bahreini, R., Conant, W. C., Jonsson, H., et al. (2007). Aerosol-cloud drop concentration closure for clouds sampled during the international consortium for atmospheric research on transport and transformation 2004 campaign. *Journal of Geophysical Research: Atmospheres*, 112(D10), D10S30. <https://doi.org/10.1029/2006JD007272>
- Garrett, J. R. (1992). *The atmospheric boundary layer*. Cambridge University Press.
- Gelaro, R., McCarty, W., Suárez, M. J., Todling, R., Molod, A., Takacs, L., et al. (2017). The modern-era retrospective analysis for research and applications, version 2 (MERRA-2). *Journal of Climate*, 30(14), 5419–5454. <https://doi.org/10.1175/JCLI-D-16-0758.1>
- Gottelman, A., & Morrison, H. (2015). Advanced two-moment bulk microphysics for global models. Part I: Off-line tests and comparison with other schemes. *Journal of Climate*, 28(3), 1268–1287. <https://doi.org/10.1175/jcli-d-14-00102.1>
- Golaz, J.-C., Larson, V. E., & Cotton, W. R. (2002). A PDF-based model for boundary layer clouds. Part I: Method and model description. *Journal of the Atmospheric Sciences*, 59(24), 3540–3551. [https://doi.org/10.1175/1520-0469\(2002\)059<3540:apbmf>2.0.co;2](https://doi.org/10.1175/1520-0469(2002)059<3540:apbmf>2.0.co;2)
- Grossman, R. L., & Betts, A. K. (1990). Air-sea interaction during an extreme cold air outbreak from the eastern coast of the United States. *Monthly Weather Review*, 118(2), 324–342. [https://doi.org/10.1175/1520-0493\(1990\)118<0324:aidaac>2.0.co;2](https://doi.org/10.1175/1520-0493(1990)118<0324:aidaac>2.0.co;2)
- Holtzlag, A. A. A., & Boville, B. A. (1993). Local versus nonlocal boundary-layer diffusion in a global climate model. *Journal of Climate*, 6(10), 1825–1842. [https://doi.org/10.1175/1520-0442\(1993\)006<1825:LVNBLD>2.0.CO;2](https://doi.org/10.1175/1520-0442(1993)006<1825:LVNBLD>2.0.CO;2)
- Jen-La Plante, I., Ma, Y., Nurowska, K., Gerber, H., Khelif, D., Karpinska, K., et al. (2016). Physics of stratocumulus top (POST): Turbulence characteristics. *Atmospheric Chemistry and Physics*, 16(15), 9711–9725. <https://doi.org/10.5194/acp-16-9711-2016>
- Jia, H., Ma, X., & Liu, Y. (2019). Exploring aerosol-cloud interaction using VOCALS-REx aircraft measurements. *Atmospheric Chemistry and Physics*, 19(12), 7955–7971. <https://doi.org/10.5194/acp-19-7955-2019>
- Knop, I., Bansmer, S. E., Hahn, V., & Voigt, C. (2021). Comparison of different droplet measurement techniques in the braunschweig icing wind tunnel. *Atmospheric Measurement Techniques*, 14(2), 1761–1781. <https://doi.org/10.5194/amt-14-1761-2021>
- Kormurcu, M., Storelvmo, T., Tan, I., Lohmann, U., Yun, Y., Penner, J. E., et al. (2014). Intercomparison of the cloud water phase among global climate models. *Journal of Geophysical Research*, 119(6), 3372–3400. <https://doi.org/10.1002/2013jd021119>
- Lambert, D., Durand, P., Thoumieux, F., Bénech, B., & Druilhet, A. (1999). The marine atmospheric boundary layer during SEMAPHORE. II: Turbulence profiles in the mixed layer. *Quarterly Journal of the Royal Meteorological Society*, 125(554), 513–528. <https://doi.org/10.1002/qj.49712555408>
- Large, W. G., & Pond, S. (1982). Sensible and latent heat flux measurements over the ocean. *Journal of Physical Oceanography*, 12(5), 464–482. [https://doi.org/10.1175/1520-0485\(1982\)012<0464:salhfm>2.0.co;2](https://doi.org/10.1175/1520-0485(1982)012<0464:salhfm>2.0.co;2)
- Larson, V. E. (2017). CLUBB-SILHS: A parameterization of subgrid variability in the atmosphere. arXiv, 1711.03675v3.
- Larson, V. E., & Golaz, J.-C. (2005). Using probability density functions to derive consistent closure relationships among higher-order moments. *Monthly Weather Review*, 133(4), 1023–1042. <https://doi.org/10.1175/mwr2902.1>
- Larson, V. E., Golaz, J.-C., & Cotton, W. R. (2002). Small-scale and mesoscale variability in cloudy boundary layers: Joint probability density functions. *Journal of the Atmospheric Sciences*, 59(24), 3519–3539. [https://doi.org/10.1175/1520-0469\(2002\)059<3519:ssamvi>2.0.co;2](https://doi.org/10.1175/1520-0469(2002)059<3519:ssamvi>2.0.co;2)
- Lenschow, D. H., & Agee, E. M. (1976). Preliminary results from the air mass transformation experiment (AMTEX). *Bulletin of the American Meteorological Society*, 44(11), 1346–1355. <https://doi.org/10.1175/1520-0477-57.11.1346>
- Lenschow, D. H., Li, X. S., Zhu, C. J., & Stankov, B. B. (1988). The stably stratified boundary layer over the great plains. *Boundary-Layer Meteorology*, 42(1–2), 95–121. <https://doi.org/10.1007/bf00119878>
- Lenschow, D. H., Wyngaard, J. C., & Pennell, W. T. (1980). Mean-field and second-moment budgets in a baroclinic, convective boundary layer. *Journal of the Atmospheric Sciences*, 37(6), 1313–1326. [https://doi.org/10.1175/1520-0469\(1980\)037<1313:mfasmb>2.0.co;2](https://doi.org/10.1175/1520-0469(1980)037<1313:mfasmb>2.0.co;2)
- Li, X.-Y., Wang, H., Chen, J., Endo, S., George, G., Cairns, B., et al. (2022). Large-eddy simulations of marine boundary layer clouds associated with cold-air outbreaks during the ACTIVATE campaign. Part I: Case setup and sensitivities to large-scale forcings. *Journal of the Atmospheric Sciences*, 79, 73–100. <https://doi.org/10.1175/JAS-D-21-0123.1>
- Ma, P.-L., Harrop, B. E., Larson, V. E., Neale, R., Gettelman, A., Morrison, H., et al. (2021). Better calibration of cloud parameterizations and subgrid effects increases the fidelity of E3SM Atmosphere Model version 1 [preprint]. Geoscientific Model Development Discussions. <https://doi.org/10.5194/gmd-2021-298>
- Melfi, S. H., Spinhrne, J. D., Chou, S. H., & Palm, S. P. (1985). Lidar observations of vertically organized convection in the planetary boundary-layer over the ocean. *Journal of Climate and Applied Meteorology*, 24(8), 806–821. [https://doi.org/10.1175/1520-0450\(1985\)024<0806:loovoc>2.0.co;2](https://doi.org/10.1175/1520-0450(1985)024<0806:loovoc>2.0.co;2)
- Neggars, R. A. J., Ackerman, A. S., Angevine, W. M., Bazile, E., Beau, I., Blossy, P. N., et al. (2017). Single-column model simulations of subtropical marine boundary-layer cloud transitions under weakening inversions. *Journal of Advances in Modeling Earth Systems*, 9(6), 2385–2412. <https://doi.org/10.1002/2017MS001064>
- Nowak, J. L., Siebert, H., Szodry, K.-E., & Malinowski, S. (2021). Coupled and decoupled stratocumulus-topped boundary layers: Turbulence properties. *Atmospheric Chemistry and Physics*, 21, 10965–10991. <https://doi.org/10.5194/acp-21-10965-2021>
- Painemal, D., Corral, A. F., Sorooshian, A., Brunke, M. A., Chellappan, S., Afzali Goroooh, V., et al. (2021). An overview of atmospheric features over the western north Atlantic ocean and north American East Coast—Part 2: Circulation, boundary layer, and clouds. *Journal of Geophysical Research: Atmospheres*, 126(6), e2020JD033423. <https://doi.org/10.1029/2020JD033423>
- Pasquier, J. R. M., & Jonas, P. R. (1998). Turbulent transport in fields of warm cumulus clouds. *Quarterly Journal of the Royal Meteorological Society*, 124(546), 363–387. <https://doi.org/10.1002/qj.49712454602>
- Prabakaran, P., Shawon, A. S. M., Kinney, G., Thomas, S., Cantrell, W., & Shaw, R. A. (2020). The role of turbulent fluctuations in aerosol activation and cloud formation. *Proceedings of the U.S. National Academy of Science*, 117(29), 16831–16838. <https://doi.org/10.1073/pnas.2006426117>
- Raes, F., Van Dingenen, R., Cuevas, E., Van Velthoven, P. F. J., & Prospiero, J. M. (1997). Observations of aerosols in the free troposphere and marine boundary layer of the subtropical north east Atlantic: Discussion of processes determining their size distribution. *Journal of Geophysical Research*, 102(D17), 21315–21328. <https://doi.org/10.1029/97jd01122>
- Sardina, G., Poulain, S., Brandt, L., & Caballero, R. (2018). Broadening of cloud droplet size spectra by stochastic condensation: Effects of mean updraft velocity and CCN activation. *Journal of the Atmospheric Sciences*, 75(2), 451–467. <https://doi.org/10.1175/JAS-D-17-0241.1>

- Scarino, A. J., Obland, M. D., Fast, J. D., Burton, S. P., Ferrare, R. A., Hostetler, C. A., et al. (2014). Comparison of mixed layer heights from airborne high spectral resolution lidar, ground-based measurements, and WRF-Chem Model during CalNex and CARES. *Atmospheric Chemistry and Physics*, *14*(11), 5547–5560. <https://doi.org/10.5194/acp-14-5547-2014>
- Seethala, C., Zuidema, P., Edson, J., Brunke, M., Chen, G., Li, X.-Y., et al. (2021). On assessing ERA5 and MERRA2 representations of cold-air outbreaks across the Gulf Stream. *Geophysical Research Letters*, *48*(19), e2021GL094364. <https://doi.org/10.1029/2021GL094364>
- Seinfeld, J. H., Bretherton, C., Carslaw, K. S., Coe, H., DeMott, P. J., Dunlea, E. J., et al. (2016). Improving our fundamental understanding of the role of aerosol-cloud interactions in the climate system. *Proceedings of the U.S. National Academy of Science*, *113*(21), 5781–5790. <https://doi.org/10.1073/pnas.1514043113>
- Siebesma, A. P., Soares, P. M. M., & Teixeira, J. (2007). A combined eddy-diffusivity mass-flux approach for the convective boundary layer. *Journal of the Atmospheric Sciences*, *64*(4), 1230–1248. <https://doi.org/10.1175/JAS3888.1>
- Skamarock, W. C., Klemp, J. B., Dudhia, J., Gill, D. O., Liu, Z., Berner, J., et al. (2019). A description of the advanced research WRF model version 4. *NCAR Tech Note NCAR/TN-556+STR*, 145. <https://doi.org/10.5065/1dfh-6p97>
- Snider, J. R., Guibert, S., Brenguier, J.-L., & Putaud, J.-P. (2003). Aerosol activation in marine stratocumulus clouds: 2. Köhler and parcel theory closure studies. *Journal of Geophysical Research: Atmospheres*, *108*(D15), 8629. <https://doi.org/10.1029/2002JD002692>
- Sorooshian, A., Anderson, B., Bauer, S. E., Braun, R. A., Cairns, B., Crosbie, E., et al. (2019). Aerosol-cloud-meteorology interaction airborne field investigations: Using lessons learned from the U.S. West Coast in the design of ACTIVATE off the U.S. East Coast. *Bulletin of the American Meteorological Society*, *100*(8), 1511–1528. <https://doi.org/10.1175/bams-d-18-0100.1>
- Sorooshian, A., Corral, A. F., Braun, R. A., Cairns, B., Crosbie, E., Ferrare, R., et al. (2020). Atmospheric research over the Western North Atlantic Ocean region and north American East Coast: A review of past work and challenges ahead. *Journal of Geophysical Research: Atmospheres*, *125*(6), e2019JD031626. <https://doi.org/10.1029/2019JD031626>
- Sullivan, S. C., Lee, D., Oreopoulos, L., & Nenes, A. (2016). Role of updraft velocity in temporal variability of global cloud hydrometeor number. *Proceedings of the U.S. National Academy of Science*, *113*(21), 5791–5796. <https://doi.org/10.1073/pnas.1514039113>
- Teixeira, J., Piepmeyer, J. R., Nehrir, A. R., Ao, C. O., Chen, S. S., Clayson, C. A., et al. (2020). Toward a global planetary boundary layer observing system: The NASA PBL incubation study team report.
- Thornhill, K. L., Anderson, B. E., Barrick, J. D. W., Bagwell, D. R., Friesen, R., & Lenschow, D. H. (2003). Air motion intercomparison flights during transport and chemical evolution in the Pacific (TRACE-P)/ACE-ASIA. *Journal of Geophysical Research*, *108*(D20), 9001. <https://doi.org/10.1029/2002JD003108>
- Tjernström, M. (1993). Turbulence length scales in stably stratified free shear flow analyzed from slant aircraft profiles. *Journal of Applied Meteorology*, *32*(5), 948–963. [https://doi.org/10.1175/1520-0450\(1993\)032<0948:tlssiss>2.0.co;2](https://doi.org/10.1175/1520-0450(1993)032<0948:tlssiss>2.0.co;2)
- Tornow, F., Ackerman, A. S., & Fridland, A. M. (2021). Preconditioning of overcast-to-broken cloud transitions by riming in marine cold air outbreaks. *Atmospheric Chemistry and Physics*, *21*(15), 12049–12067. <https://doi.org/10.5194/acp-21-12049-2021>
- Tornow, F., Ackerman, A. S., Fridlind, A. M., Cairns, B., Crosbie, E. C., Kirschler, S., et al. (2022). Dilution of boundary layer cloud condensation nucleus concentrations by free tropospheric entrainment during marine cold air outbreaks. *Geophysical Research Letters*, *49*(11), e2022L09844. <https://doi.org/10.1029/2022GL09844>
- Tselioudis, G., Rossow, W., Zhang, Y. C., & Konsta, D. (2013). Global weather states and their properties from passive and active satellite cloud retrievals. *Journal of Climate*, *26*(19), 7734–7746. <https://doi.org/10.1175/jcli-d-13-00024.1>
- Twomey, S. (1977). The influence of pollution on the shortwave albedo of clouds. *Journal of the Atmospheric Sciences*, *34*(7), 1149–1152. [https://doi.org/10.1175/1520-0469\(1977\)034<1149:tiopot>2.0.co;2](https://doi.org/10.1175/1520-0469(1977)034<1149:tiopot>2.0.co;2)
- van der Dussen, J. J., de Ronde, S. R., Ackerman, A. S., Blossey, P. N., Bretherton, C. S., Kurowski, M. J., et al. (2013). The GASS/EUCLIPSE model intercomparison of the stratocumulus transition as observed during ASTEX: LES results. *Journal of Advances in Modeling Earth Systems*, *5*(3), 483–499. <https://doi.org/10.1002/jame.20033>
- Van Dingenn, R., Virkkula, A. O., Raes, F., Bates, T. S., & Wiedensohler, A. (2000). A simple non-linear analytical relationship between aerosol accumulation number and sub-micron volume, explaining their observed ratio in the clean and polluted marine boundary layer. *Tellus*, *52B*(2), 439–451. <https://doi.org/10.1034/j.1600-0889.2000.00091.x>
- Vukovich, F. M., Dunn, J. W., & Crissman, B. W. (1991). Aspects of the evolution of the marine boundary-layer during cold-air outbreaks off the southeast coast of the United States. *Monthly Weather Review*, *119*(9), 2252–2279. [https://doi.org/10.1175/1520-0493\(1991\)119<2252:aoteot>2.0.co;2](https://doi.org/10.1175/1520-0493(1991)119<2252:aoteot>2.0.co;2)
- Wang, H., & Feingold, G. (2009). Modeling mesoscale cellular structures and drizzle in marine stratocumulus. Part I: Impact of drizzle on the formation and evolution of open cells. *Journal of the Atmospheric Sciences*, *66*(11), 3237–3256. <https://doi.org/10.1175/2009JAS3022.1>
- Zhang, G. J., & McFarlane, N. A. (1995). Sensitivity of climate simulations to the parameterization of cumulus convection in the Canadian climate centre general circulation model. *Atmosphere-Ocean*, *33*(3), 407–446. <https://doi.org/10.1080/07055900.1995.9649539>
- Zhang, Y., Rosenfeld, D., & Li, Z. (2021). Sub-cloud turbulence explains cloud-base updrafts for shallow cumulus ensembles: First observational evidence. *Geophysical Research Letters*, *48*(6), e2020GL091881. <https://doi.org/10.1029/2020GL091881>
- Zheng, X., Klein, S. A., Ghate, V. P., Santos, S., McGibbon, J., Caldwell, P., et al. (2020). Assessment of precipitating marine stratocumulus clouds in the E3SMv1 atmosphere model: A case study from the ARM MAGIC field campaign. *Monthly Weather Review*, *148*(8), 3341–3359. <https://doi.org/10.1175/MWR-D-19-0349.1>